

This document is the Accepted Manuscript version of a Published Work that appeared in final form in Applied Catalysis B: Environmental 237 (2018) 844–854, after peer review and technical editing by the publisher. To access the final edited and published work see <https://doi.org/10.1016/j.apcatb.2018.06.050>

OXIDATION OF RESIDUAL METHANE FROM VNG VEHICLES OVER  $\text{CO}_3\text{O}_4$ -BASED  
CATALYSTS: COMPARISON AMONG BULK,  $\text{Al}_2\text{O}_3$ -SUPPORTED AND Ce-DOPED  
CATALYSTS

A. Choya, B. de Rivas, J.R. González-Velasco, J.I. Gutiérrez-Ortiz, R. López-Fonseca

Applied Catalysis B: Environmental 237 (2018) 844–854

DOI: 10.1016/j.apcatb.2018.06.050

©2018. This manuscript version is made available under the CC-BY-NC-ND 4.0 license  
<https://creativecommons.org/licenses/by-nc-nd/4.0/>

1     **OXIDATION OF RESIDUAL METHANE FROM VNG VEHICLES**  
2             **OVER C<sub>03</sub>O<sub>4</sub>-BASED CATALYSTS: COMPARISON AMONG**  
3             **BULK, Al<sub>2</sub>O<sub>3</sub>-SUPPORTED AND Ce-DOPED CATALYSTS**

4

5                     Andoni Choya, Beatriz de Rivas, Juan Ramón González-Velasco

6                             Jose Ignacio Gutiérrez-Ortiz, Rubén López-Fonseca\*

7

8                     Chemical Technologies for Environmental Sustainability Group,

9                     Department of Chemical Engineering, Faculty of Science and Technology,

10             University of the Basque Country UPV/EHU, PO Box 644, E-48080 Bilbao, Spain

11

12

13             \*Corresponding author:

14                     Phone: +34-94-6013485

15                     Fax: +34-94-6015963

16                     E-mail address: [ruben.lopez@ehu.eus](mailto:ruben.lopez@ehu.eus)

17

18 **ABSTRACT**

19 Cobalt oxide based catalysts with three different active phase configurations, namely  
20 bulk, alumina supported and cerium-doped  $\text{Co}_3\text{O}_4$  samples were examined for the  
21 complete oxidation of methane under conditions similar to those found in the exhaust of  
22 VNG engines. The structural and redox properties of the resulting catalysts were  
23 determined by  $\text{N}_2$  adsorption-desorption, WDXRF, ICP-AES, X-Ray diffraction,  
24 temperature-programmed reactions, UV-vis-NIR DRS, XPS and Raman spectroscopy.  
25 Alumina-supported catalysts (10–40%wt. Co) were found to be less active, since the  
26 strong interactions between the alumina and the  $\text{Co}_3\text{O}_4$  active phase were highly  
27 detrimental for the redox properties of these catalysts. On the other hand, doping with  
28 cerium (10%wt.) led to an increased inherent activity of the  $\text{Co}_3\text{O}_4$  phase by distorting  
29 the spinel lattice, which resulted in improved structural and redox properties and  
30 enhanced mobility of the oxygen species within the spinel lattice. These catalysts were  
31 also stable over a prolonged period of time under both dry and humid conditions (150  
32 hours).

33

34 *Keywords: catalytic combustion, methane, cobalt oxide, cerium doping, oxygen mobility*

35

## 36 **1. Introduction**

37 The use of natural gas as fuel for vehicles (also known as Vehicular Natural Gas or VNG)  
38 is considered a reliable alternative, with a well-established technology, that can serve as  
39 a transition technology in the way to cleaner H<sub>2</sub>-based energy sources. VNG engines are  
40 between 10-20% more efficient than gasoline or diesel engines and have a lower  
41 environmental impact with limited NO<sub>x</sub> and soot emissions [1-4]. Their main technical  
42 limitation lies in the release of residual methane, not burned in the engine, which is a  
43 powerful greenhouse effect gas.

44 Catalytic oxidation constitutes an attractive post-treatment strategy to convert methane  
45 into CO<sub>2</sub> and water. Unfortunately, it is a noticeably demanding process compared with  
46 the oxidation of other hydrocarbons such as propane or butane, due to its high chemical  
47 stability. This low reactivity determines the temperature of the process, which should not  
48 exceed a temperature threshold of 500 °C, since that is the thermal level of the exhaust  
49 gases from the engine. The mostly used catalysts on a commercial scale for VNG vehicles  
50 are based on supported noble metals, mainly palladium [5,6]. However, these catalysts,  
51 which can contain up to a 4% in weight of palladium, are expensive while their behaviour  
52 is negatively influenced by sintering and the presence of water in the reaction stream  
53 [7,8]. In this context, finding cheaper, alternative catalysts with an appropriate  
54 performance has become an interesting challenge that has the potential to reduce the cost  
55 of post-treatment systems for exhaust gases and contribute to increase the attractiveness  
56 of VNG engines as well.

57 Cobalt spinel oxides, like Co<sub>3</sub>O<sub>4</sub>, have been demonstrated to exhibit a high activity for  
58 methane catalytic combustion, and are therefore considered good alternative candidates  
59 to noble metal based catalysts, owing to their relatively low cost, high thermal and  
60 hydrothermal stability and selectivity to CO<sub>2</sub> [9,10]. However, the specific

61 physicochemical properties of these catalysts are highly dependent on the specific  
62 configuration of the active phase, that is, whether the  $\text{Co}_3\text{O}_4$  is a bulk phase, supported  
63 on a porous media, or mixed with other elements. Pure bulk  $\text{Co}_3\text{O}_4$  catalysts take  
64 advantage of the excellent redox properties of this material, which allow for a good  
65 mobility of the oxygen species and reducibility. However, their structural properties are  
66 usually very poor when using conventional synthesis methodologies (precipitation or  
67 direct calcination), with low specific surface areas and large crystallite sizes [11,12].  
68 Better textural properties can be obtained with solvothermal or hard-template-based  
69 routes [13-16]. In a simpler way, an increased available metallic surface area and  
70 improved structural properties can be obtained by depositing the  $\text{Co}_3\text{O}_4$  phase over the  
71 surface of a porous media. This strategy has been reported to enhance the inherent  
72 catalytic activity of  $\text{Co}_3\text{O}_4$  in some cases [17,18], but, in other cases, the interactions  
73 between cobalt oxide and the support can be detrimental owing to their negative impact  
74 on the redox properties [19]. For example, when alumina is used as a support the  
75 formation of  $\text{CoAl}_2\text{O}_4$  often occurs. This undesired phase fix a certain amount of cobalt  
76 species due to its high stability. Therefore, a fraction of deposited cobalt species is not  
77 able to participate in the  $\text{Co}^{3+}/\text{Co}^{2+}$  redox cycle. On the other hand, doping the bulk  $\text{Co}_3\text{O}_4$   
78 with another metallic element can improve its textural and redox properties [20,21]. The  
79 properties of the resultant catalysts strongly depend on various parameters such as the  
80 composition or the presence of segregated or undesired phases [22].  
81 Up to now, various cobalt-based catalysts with the described three configurations have  
82 been profusely examined for the complete oxidation of methane [9,17,23-28]. However,  
83 the different routes employed for catalysts synthesis and the wide range of operation  
84 conditions chosen for catalytic evaluation make the comparison of their corresponding  
85 performance and properties a particularly difficult task [29]. To the best of our

86 knowledge, no systematic analysis of the three type of catalysts under the same conditions  
87 has ever been attempted. Thus, in the present work, these three configurations have been  
88 implemented for the design of  $\text{Co}_3\text{O}_4$  catalysts for methane catalytic oxidation. More  
89 specifically, various bulk  $\text{Co}_3\text{O}_4$  samples were prepared by simple calcination and  
90 precipitation. Secondly, a series of  $\text{Co}_3\text{O}_4$  catalysts supported on alumina with varying  
91 cobalt content in the range 10–40%wt. were examined. Lastly, as for doped  $\text{Co}_3\text{O}_4$   
92 catalysts, several samples modified by cerium, with a content between 5 and 20%wt.,  
93 were synthesised. Along with a detailed characterisation of the physicochemical  
94 properties of these catalysts, by means of a wide number of analytical techniques  
95 including BET measurements, XRD, WDXRF, ICP-AES, UV-vis-NIR DRS, Raman  
96 spectroscopy, XPS,  $\text{H}_2$ -TPR and  $\text{CH}_4$ -TPRe, this work presents kinetic data that were  
97 correlated with the key catalytic properties of each type of catalyst. Also, attention has  
98 been paid to examining the catalytic stability during a prolonged time interval under both  
99 dry and humid conditions.

100

## 101 **2. Experimental**

### 102 *2.1. Catalysts preparation*

103 Bulk  $\text{Co}_3\text{O}_4$  catalysts were prepared following two different routes, already described  
104 elsewhere [30]. The first route was a simple calcination in static air of two different cobalt  
105 precursors, namely cobalt (II) nitrate hexahydrate ( $\text{Co}(\text{NO}_3)_2 \cdot 6\text{H}_2\text{O}$ , Sigma-Aldrich) and  
106 cobalt (II) hydroxycarbonate ( $2\text{CoCO}_3 \cdot 3\text{Co}(\text{OH})_2 \cdot x\text{H}_2\text{O}$ , Panreac). The resulting samples  
107 were denoted as DC and HC, respectively. The second route consisted of an aqueous basic  
108 precipitation of a cobalt precursor, resulting in the formation of cobalt hydroxycarbonate.  
109 A solution of  $\text{Na}_2\text{CO}_3$  1.2M was added drop-by-drop to 100 mL of  $\text{Co}(\text{NO}_3)_2 \cdot 6\text{H}_2\text{O}$  0.5M,  
110 while the temperature was kept constant at 80 °C, until pH 8.5 was attained. The obtained

111 precipitates were collected and washed thoroughly with at least 5 litres of water, to wash  
112 off all the sodium ions which are known to be especially detrimental for the activity of  
113 oxidation catalysts [31]. The sample was labelled as CC. Finally, a commercial bulk  
114  $\text{Co}_3\text{O}_4$  sample (Alfa Aesar) was used as reference. This sample was denoted as COM.  
115 Supported  $\text{Co}_3\text{O}_4/\text{Al}_2\text{O}_3$  catalysts were prepared by a precipitation route following the  
116 same methodology as the CC catalyst, but adding  $\gamma\text{-Al}_2\text{O}_3$  (Saint Gobain Norpro SA  
117 6173), previously stabilized at 850 °C for 4 h in static air. The selected metallic Co  
118 loadings were 10, 20, 30, 35 and 40wt%. These samples were denoted as  $x\text{Co}/\text{Al}_2\text{O}_3$   
119 where x stands for the nominal cobalt loading. For comparative purposes, a bulk  $\text{CoAl}_2\text{O}_4$   
120 sample was also obtained by a precipitation route, where a cobalt salt ( $\text{Co}(\text{NO}_3)_2 \cdot 6\text{H}_2\text{O}$ )  
121 and an aluminium salt ( $\text{Al}(\text{NO}_3)_3 \cdot 9\text{H}_2\text{O}$ ) with stoichiometric proportions were  
122 precipitated by the drop-by-drop addition of  $\text{Na}_2\text{CO}_3$  1.2M, until pH 9 was achieved.  
123 Cerium-doped bulk  $\text{Co}_3\text{O}_4$  catalysts were prepared by a precipitation route, similar to the  
124 route followed for the synthesis of the CC sample, but starting from adjusted mixtures of  
125  $\text{Ce}(\text{NO}_3)_3 \cdot 6\text{H}_2\text{O}$  and  $\text{Co}(\text{NO}_3)_2 \cdot 6\text{H}_2\text{O}$  to obtain catalysts with nominal cerium loadings of  
126 5, 10, 15 and 20wt%, which corresponded to Ce/Co molar ratios of 0.03, 0.06, 0.10 and  
127 0.14, respectively. The samples were named as  $x\text{Ce}/\text{Co}_3\text{O}_4$  where x is the nominal cerium  
128 content. In addition, a sample of pure  $\text{CeO}_2$  was prepared using the same route. Again,  
129 the obtained precipitates were collected and washed thoroughly with water. All catalyst  
130 precursors were dried in static air at 110 °C for 16 hours and subjected to calcination in  
131 static air to produce the final catalysts. The calcination protocol was defined on the basis  
132 of the results obtained from a previous thermogravimetric analysis over the catalyst  
133 precursors, and involved three heating steps, separated by 30-minute isotherms: an initial  
134 step at 5 °C  $\text{min}^{-1}$  from room temperature to 125 °C, an intermediate step at 1 °C  $\text{min}^{-1}$

135 until 300 °C and a final step at 5 °C min<sup>-1</sup> until 600 °C, which was then maintained for 4  
136 hours. Exceptionally, the bulk CoAl<sub>2</sub>O<sub>4</sub> sample was also calcined at 850 °C.

## 137 2.2. *Characterisation techniques*

138 Textural properties of the catalysts were determined from the nitrogen-adsorption  
139 isotherms at -196 °C obtained with a Micromeritics TriStar II apparatus. The specific  
140 surface of the samples was obtained by the BET method, and the average pore size was  
141 calculated using the BJH method. All samples were degassed prior to analysis on a  
142 Micromeritics SmartPrep apparatus at 300 °C for 10 hours with a N<sub>2</sub> flow.

143 The composition of the supported Co<sub>3</sub>O<sub>4</sub>/Al<sub>2</sub>O<sub>3</sub> catalysts and the CoAl<sub>2</sub>O<sub>4</sub> samples was  
144 determined by Wavelength Dispersive X-Ray Fluorescence (WDXRF). From each  
145 sample in powder form, a boron glass pearl was prepared by fusion in an induction micro-  
146 furnace, by mixing the sample with the flux agent Spectromelt A12 (Merck) in an  
147 approximate proportion of 20:1. Chemical analysis of each pearl was performed under  
148 vacuum, using a PANalytical AXIOS sequential WDXRF spectrometer, equipped with a  
149 Rh tube and three different detectors (gas flow, scintillation and Xe sealed). The  
150 composition of Ce-doped catalysts was determined by ICP-AES in a Thermo Elemental  
151 Iris Intrepid apparatus. The pretreatment involved the acid digestion of 5-10 mg of each  
152 sample, followed by dissolution in 100 mL of Milli-Q water.

153 Structural properties of the catalysts were determined by X-Ray diffraction. XRD analysis  
154 were performed on a X'PERT-PRO X-Ray diffractometer using Cu K $\alpha$  radiation ( $\lambda =$   
155 1.5406 Å) and a Ni filter. The X-Ray tube was operated at 40 kV and 40 mA of current.  
156 The samples were scanned from an initial value of  $2\theta = 5^\circ$  to a final value of  $2\theta = 80^\circ$ ,  
157 with a step size of 0.026° and a counting time of 2.0 seconds for each step. Phase  
158 identification was performed by comparison of the obtained diffraction patterns with  
159 JCPDS (Joint Committee on Powder Diffraction Standards) database cards. Occasionally,

160 a longer counting time (26.8 s) was applied to perform a detailed XRD analysis over the  
161 supported  $\text{Co}_3\text{O}_4/\text{Al}_2\text{O}_3$  and Ce-doped catalysts. The cell size of the  $\text{Co}_3\text{O}_4$  phase was  
162 obtained by profile matching of the detailed XRD patterns using FullProf.2k software.  
163 Redox properties and Co species distribution was investigated by means of different  
164 techniques. Temperature-programmed reduction with hydrogen ( $\text{H}_2$ -TPR) was performed  
165 on a Micromeritics Autochem 2920 apparatus, using a 5%  $\text{H}_2/\text{Ar}$  mixture as the reducing  
166 gas. The analysis protocol involved an initial pre-treatment step with a 5%  $\text{O}_2/\text{He}$  mixture  
167 at 300 °C for 30 minutes. The aim of this step was to remove impurities and/or water that  
168 could be retained on the surface of the samples while at the same time fully restoring the  
169 oxygen vacancies of the spinel lattice before the analysis of the reducibility. After cooling  
170 down to room temperature with flowing He, the TPR experiment was performed, up to  
171 600 °C for the bulk  $\text{Co}_3\text{O}_4$  catalysts, 950 °C for the supported  $\text{Co}_3\text{O}_4/\text{Al}_2\text{O}_3$  catalysts and  
172  $\text{CoAl}_2\text{O}_4$  samples and 900 °C for the Ce-doped  $\text{Co}_3\text{O}_4$  catalysts. The corresponding final  
173 temperature was then maintained for 30 minutes. The water produced throughout the  
174 whole experiment was eliminated using a cold trap, to avoid interference with the TCD  
175 detector. Additional information regarding the reducibility of the catalysts was obtained  
176 by means of temperature programmed reaction with a 5%  $\text{CH}_4/\text{He}$  mixture in the absence  
177 of oxygen ( $\text{CH}_4$ -TPRe) coupled to mass spectrometry (MKS Cirrus Quadrupole Mass  
178 Spectrometer).  
179 X-Ray photoelectron spectroscopy (XPS) analysis was performed using a SPECS system  
180 equipped with a Phoibos 150 1D analyzer and a DLD-monochromatic radiation source.  
181 UV-vis-NIR diffuse reflectance (DRS) spectra of the samples was obtained on a Jasco V-  
182 570 apparatus in the 200-2300 nm wavelength range. The analysis by Raman  
183 spectroscopy was carried out by using a Renishaw InVia Raman spectrometer, coupled  
184 to a Leica DMLM microscope. The excitation wavelength was 514 nm (ion-argon laser,

185 Modu-Laser). The spatial resolution was 2 microns. For each spectrum 20 seconds were  
186 employed and 5 scans were accumulated with the 10% of the maximum power of the 514  
187 nm laser in a spectral window of 150-1200  $\text{cm}^{-1}$ .

188

### 189 2.3. *Catalytic activity determination*

190 Catalytic activity tests were performed in a bench-scale fixed bed reactor, Microactivity  
191 modular laboratory system manufactured by PID Eng&Tech S.L., operated at  
192 atmospheric pressure and monitored by computer. The reactor was a stainless steel  
193 (Hasteloy X) tube, manufactured by Autoclave Engineers, with an internal diameter of  
194 8.55 mm and a length of 305 mm. The temperature inside the reactor was measured by a  
195 multipoint K type thermocouple placed in the catalyst bed. For each reaction experiment,  
196 1 g of catalyst granulated to a particle size of 0.25–0.3 mm was loaded into the reactor,  
197 diluted with 1 g of inert quartz granulated to a particle size of 0.5–0.8 mm to improve gas  
198 flow and heat distribution along the bed and avoid diffusional effects affecting the  
199 reaction rate. A reactor diameter/particle diameter ratio (31) higher than 10 and a catalytic  
200 bed length/particle diameter ratio (79) higher than 50 ensured that both by-pass and axial  
201 dispersion effects could be neglected (Table S1, Supplementary material) Thus, an ideal  
202 plug-flow in the reactor could be supposed.

203 The feed consisted of a gaseous mixture of 1%CH<sub>4</sub>, 10%O<sub>2</sub> and N<sub>2</sub> as the balance gas.

204 The selected composition of the gas feed was comparable to that found in the exhaust of  
205 VNG engines, which typically contains 0.5-1%CH<sub>4</sub> and 5-10%O<sub>2</sub>. A total gas flow of  
206 500  $\text{cm}^3 \text{min}^{-1}$  was used, which corresponded to a gas hourly space velocity of 60,000  $\text{h}^{-1}$   
207 approximately (300 mL CH<sub>4</sub>  $\text{g}^{-1} \text{h}^{-1}$ ). Catalytic activity was measured from 200 to  
208 600 °C. Conversion measurements and product profiles were taken at steady state each  
209 25 °C, typically after 15 minutes on stream. The furnace temperature was programmed in

210 a stepwise progression. Each temperature level was attained using a heating ramp of 1 °C  
211 min<sup>-1</sup>. Additionally, stability tests (1%CH<sub>4</sub>, 10%O<sub>2</sub> and N<sub>2</sub> as the balance gas) in the  
212 presence (10%H<sub>2</sub>O) or absence of water vapour were carried out for a total time on stream  
213 of 150 h at 450 °C. Methane conversion was calculated by the difference between inlet  
214 and outlet CH<sub>4</sub> concentrations. Inlet and outlet streams were analysed using an on-line  
215 Agilent Technologies 7890N gas chromatograph equipped with a thermal conductivity  
216 detector (TCD) and two columns: a PLOT 5A molecular sieve column for the analysis of  
217 CH<sub>4</sub>, O<sub>2</sub>, N<sub>2</sub> and CO; and a PLOT U column for CO<sub>2</sub> analysis. Each chromatographic  
218 analysis was performed in triplicate in order to check reproducibility, which was below  
219 1%. To ensure that the obtained catalytic results were not affected by both mass and heat  
220 transfer limitations, the criteria for intra-granular and extra-granular mass diffusion,  
221 energy diffusion and temperature gradients were checked to be above the limit, according  
222 to the Eurokin procedure [32,33]. It was therefore considered that catalytic activity results  
223 were not significantly influenced by interphase transportation. The calculations are  
224 summarised in Table S1 (Supplementary material).

225

### 226 **3. Results and Discussion**

#### 227 *3.1. Evaluation of bulk Co<sub>3</sub>O<sub>4</sub> catalysts*

228 The textural properties of the bulk Co<sub>3</sub>O<sub>4</sub> samples in terms of BET surface area, pore  
229 mean diameter and pore volume are shown in Table 1. The surface area varied between  
230 5 m<sup>2</sup> g<sup>-1</sup> over the DC sample and 14 m<sup>2</sup> g<sup>-1</sup> over the CC sample. This latter oxide also  
231 exhibited the largest pore volume and smallest pore diameter, thus suggesting that the CC  
232 route produces samples with better textural properties. The structural properties were  
233 characterised by XRD, using the JCDPS files as a reference. For every sample, all  
234 diffraction peaks, located at 19.0°, 31.3°, 36.8°, 44.8°, 59.4° and 65.2°, could be assigned

235 to a pure phase of mixed cobalt (II,III) oxide with spinel structure (JCPDS 42-1467). The  
236 crystallite size, also included in Table 1, was estimated from the Full Width Half  
237 Maximum (FWHM) of the characteristic peak located at  $36.8^\circ$ , which corresponded to  
238 the (311) plane, by applying the Scherrer equation. It was found that the crystallite sizes,  
239 in the 63–84 nm range, inversely correlated to their specific surface area. This relationship  
240 was explained in terms of small  $\text{Co}_3\text{O}_4$  crystallites exposing higher surfaces than larger  
241 ones [34,35].

#### 242 TABLE 1

243 The redox properties of  $\text{Co}_3\text{O}_4$  were investigated by means of  $\text{H}_2$ -TPR. For all samples  
244 the hydrogen consumption profiles (Figure 1) were relatively similar, showing a two-step  
245 reduction process. The first hydrogen consumption peak, centred at  $310^\circ\text{C}$ , was assigned  
246 to the reduction of  $\text{Co}^{3+}$  to  $\text{Co}^{2+}$ ; whilst the second reduction peak, located between  $325$   
247 and  $425^\circ\text{C}$ , was attributed to the reduction of  $\text{Co}^{2+}$  to metallic Co [36]. No other hydrogen  
248 consumption was detected over  $500^\circ\text{C}$ . It was therefore confirmed that the only reducible  
249 phase present in all samples was  $\text{Co}_3\text{O}_4$ . After integration and quantitative evaluation of  
250 the TPR profiles, the specific hydrogen uptake of each reduction step and the  
251 corresponding ratio were computed, as shown in Table 1. The specific consumption of  
252 the synthesised oxides was very similar to the theoretical value ( $16.6\text{ mmol g}^{-1}$ ). As for  
253 the ratio between the two uptakes, the CC sample gave the highest value (0.35). This was  
254 slightly higher than the theoretical ratio (0.33)

#### 255 FIGURE 1

256 On the other hand, XPS analysis could provide useful information about the distribution  
257 of the reducible species on the surface of the spinel. For all bulk  $\text{Co}_3\text{O}_4$  samples, Co 2p  
258 spectra (Figure S1, Supplementary material) showed broad signals, thus suggesting the  
259 presence of various cobalt species on the surface. In particular, the Co  $2p_{3/2}$  signal could

260 be deconvoluted in at least five different contributions [37,38]. Hence, the two signals  
261 located at lower binding energies, namely 779.5 and 780.7 eV, were attributed to  $\text{Co}^{3+}$   
262 and  $\text{Co}^{2+}$  cations associated with oxide  $\text{O}^{2-}$  anions, respectively, while the signal centred  
263 at about 782.7 eV was attributed to the presence of CoO species on the surface. The  
264 presence of this species was comparable on the four samples, around 5–10% of the total  
265 amount of cobalt. Finally, the two signals located at higher binding energies (785.5 and  
266 789.5 eV) were identified as the satellite signals from  $\text{Co}^{2+}$  and  $\text{Co}^{3+}$  ions, respectively  
267 [39]. The O 1s spectra showed two different signals located at 529.8 and 530.8 eV,  
268 respectively. The former was assigned to oxygen ions from the lattice ( $\text{O}_{\text{latt}}$ ) while the  
269 latter was attributed to adsorbed oxygen species on the surface ( $\text{O}_{\text{ads}}$ ) [40]. From the  
270 quantification of the signals, the  $\text{Co}^{3+}/\text{Co}^{2+}$  and  $\text{O}_{\text{ads}}/\text{O}_{\text{latt}}$  molar ratios (Table 1) could be  
271 calculated. The relationship shown in Figure 2 evidenced that the higher the surface  
272  $\text{Co}^{3+}/\text{Co}^{2+}$  molar ratio, the higher the concentration of lattice oxygen species [37].

## 273 FIGURE 2

274 The catalytic activity of each bulk  $\text{Co}_3\text{O}_4$  catalyst for the complete oxidation of methane  
275 was assessed by defining their respective light-off curves. Since the calcination process  
276 would stabilize the catalysts up to the calcination temperature, light-off curves were taken  
277 between 200 and 600 °C. For each sample, three consecutive tests were performed. In all  
278 cases, the second and third cycles were characterised by an identical light-off curve  
279 (Figure 3). This revealed that the first cycle worked as a ‘conditioning’ cycle and, after  
280 that, the catalysts became stable under the employed reaction conditions. On the basis of  
281 the  $T_{50}$  (temperature required for 50% conversion) values the following trend was noticed:  
282  $\text{CC} > \text{COM} > \text{HC} > \text{DC}$ . This finding evidenced that precipitation was a more suitable  
283 preparation methodology for bulk oxides. Note that in all cases the selectivity to  $\text{CO}_2$  was  
284 100%. The reaction rate of the catalysts was calculated at 375 °C under differential

285 conditions, this is to say, when the methane conversion was below 20%. The estimated  
286 values were in the 1.07-1.85 mmol CH<sub>4</sub> g<sub>Co</sub><sup>-1</sup> h<sup>-1</sup> (Table 2). On the other hand, the integral  
287 method was applied to estimate the apparent activation energy when considering a first  
288 pseudo-order for methane and a zero pseudo-order for oxygen. The assumed reaction  
289 orders were compatible with Mars–van Krevelen kinetics with an excess of oxygen,  
290 which has already been proven to be the most plausible model for the catalytic oxidation  
291 of methane and other hydrocarbons [18,41]. Conversions between 10 and 90% were fit  
292 to the following linearized equation for the integral reactor (Equation 1)

$$293 \quad \ln[-\ln(1-X)] = \ln \left[ k_0 C_{CH_4} \left( \frac{W}{F_{CH_4}} \right) \right] - \frac{E_a}{RT} \quad (1)$$

294 where X is the fractional conversion of methane, k<sub>0</sub> is the pre-exponential factor of the  
295 Arrhenius equation and W/F<sub>CH<sub>4</sub></sub> is the weight hourly space velocity. The goodness of the  
296 numerical fit is shown in Figure S2 (Supplementary material) while the corresponding  
297 values for the apparent activation energy for each sample are listed in Table 2. Note that  
298 the observed values of the activation energies should be characterized as tentative since  
299 effect of the adsorption-desorption equilibrium of the formed water would be hidden into  
300 the reported value.

301 TABLE 2

302 FIGURE 3

303 The activation energy of all pure Co<sub>3</sub>O<sub>4</sub> samples were very similar (71–74 kJ mol<sup>-1</sup>) and  
304 comparable with the values reported in the literature for this reaction [42,43]. On the other  
305 hand, Figure 4 revealed that there was a good correlation between the reaction rate at  
306 375 °C and the surface Co<sup>3+</sup>/Co<sup>2+</sup> molar ratio of the samples, which in turn was related to  
307 a more active role of lattice oxygen in the reaction with respect to adsorbed species

308 [20,26,44]. The relative abundance of these catalytically active species (easily reducible  
309  $\text{Co}^{3+}$ ) was optimised for the CC sample prepared by precipitation.

310 **FIGURE 4**

311 *3.2. Characterisation of supported  $\text{Co}_3\text{O}_4/\text{Al}_2\text{O}_3$  catalysts*

312 The textural properties (BET surface area, mean pore diameter and pore volume) and Co  
313 loading of the supported  $\text{Co}_3\text{O}_4/\text{Al}_2\text{O}_3$  samples ( $x\text{Co}/\text{Al}_2\text{O}_3$ ) are shown in Table 3. The  
314 results indicated that the cobalt species deposited over the surface of the support  
315 progressively blocked its pores with increasing metallic loading, as pointed out by the  
316 observed decrease in the surface area from  $136 \text{ m}^2 \text{ g}^{-1}$  for the bare  $\gamma$ -alumina to  $84 \text{ m}^2 \text{ g}^{-1}$   
317 for the  $40\text{Co}/\text{Al}_2\text{O}_3$  catalyst. All samples presented a lower pore volume with respect to  
318 the support, and this slightly decreased with Co loading. Furthermore, as can be seen in  
319 Figure S3 (Supplementary material), all samples exhibited a pore size distribution centred  
320 at a smaller size in comparison with the pure  $\gamma$ - $\text{Al}_2\text{O}_3$ . This suggested that the addition of  
321 cobalt to the alumina gradually blocked its largest pores.

322 **TABLE 3**

323 The XRD patterns of the alumina supported  $\text{Co}_3\text{O}_4$  catalysts are shown in Figure 5. For  
324 the sake of comparison the patterns of the bare alumina support is also included. The  
325 following signals located at  $2\theta = 19.0^\circ, 31.3^\circ, 36.8^\circ, 44.8^\circ, 59.4^\circ$  and  $65.2^\circ$  were clearly  
326 visible. These could, in principle, be assigned to the  $\text{Co}_3\text{O}_4$  phase. However, the presence  
327 of  $\text{CoAl}_2\text{O}_4$  could not be ruled out since its diffraction signals are virtually identical to  
328 those of  $\text{Co}_3\text{O}_4$ . On the other hand, the signals of the support ( $2\theta = 33.0^\circ, 37.1^\circ, 39.7^\circ,$   
329  $45.6^\circ$  and  $67.3^\circ$ ) were also observed, more noticeably in the samples with a Co loading  
330 between 10 and 30% wt. On the other hand, it was clear that the crystallinity of the samples  
331 increased with the Co loading since the diffraction signals became sharper. This, in turn,  
332 would mean that the  $\text{Co}_3\text{O}_4$  crystallites became larger with Co loading, but their size could

333 not be properly estimated due to the possible interference of the  $\text{CoAl}_2\text{O}_4$  diffraction  
334 signals. However, an attempt was made to calculate the average crystallite size of the Co-  
335 phases with a spinel structure ( $\text{Co}_3\text{O}_4$  or  $\text{CoAl}_2\text{O}_4$ ). For this calculation the most intense  
336 peak of both phases ( $2\theta = 36.8^\circ$ ) was not used since it overlapped with one signal  
337 assignable to the  $\gamma$ -alumina support ( $2\theta = 37.1^\circ$ ). Accordingly, the signal at  $2\theta = 59.4^\circ$   
338 was selected for this estimation. The calculated values evidenced that crystallite size  
339 gradually increased from 13 to 35 nm with Co loading up to 35%wt. No further increase  
340 was noticed for the sample with the highest metal loading (34 nm).

#### 341 FIGURE 5

342 The structure of the samples was additionally investigated by UV-vis-NIR diffuse  
343 reflectance spectroscopy. For comparative purposes two bulk cobalt aluminate samples  
344 prepared by precipitation and calcined at 600 and 850 °C were used. The spectra of these  
345 samples along with those corresponding to the supported catalysts are shown in Figure S4  
346 (Supplementary material). For all the samples the spectra displayed three absorption  
347 bands located at 1210, 1320 and 1510 nm, consistent with tetrahedral  $\text{Co}^{2+}$  species, along  
348 with weak bands at 430 and 720 nm consistent with octahedral  $\text{Co}^{3+}$  species, both  
349 associated with free  $\text{Co}_3\text{O}_4$  [45,46]. In addition, a set of bands at 552, 585 and 630 nm,  
350 related to the presence of  $\text{CoAl}_2\text{O}_4$ , was visible in the spectra of the 10Co/ $\text{Al}_2\text{O}_3$  and  
351 20Co/ $\text{Al}_2\text{O}_3$  samples [46,47]. This finding suggested that both  $\text{Co}_3\text{O}_4$  and  $\text{CoAl}_2\text{O}_4$  were  
352 present in the supported catalysts. Also, the samples with a low Co content exhibited a  
353 band at 1930 nm associated with hydrated alumina [48].

354 The XPS spectra of the supported samples were characterised by a lower signal/noise  
355 ratio than that exhibited by bulk  $\text{Co}_3\text{O}_4$ . Hence, the deconvolution of these profiles was  
356 not possible. Nevertheless, the position of the main signal of the Co 2p spectra (Figure 6)  
357 could give some information about the nature of the cobalt species on the surface. The

358 binding energy of the 10Co/Al<sub>2</sub>O<sub>3</sub>, 20Co/Al<sub>2</sub>O<sub>3</sub> and 30Co/Al<sub>2</sub>O<sub>3</sub> catalysts increased from  
359 780.4 to 781.1–781.4 eV, thereby revealing that CoAl<sub>2</sub>O<sub>4</sub> and Co<sub>3</sub>O<sub>4</sub> coexisted on the  
360 surface, in line with the results obtained by diffuse reflectance spectroscopy. Note that  
361 the main signal of the Co 2p spectra in the bulk CoAl<sub>2</sub>O<sub>4</sub> sample calcined at 600 °C is  
362 located at 781.4 eV. By contrast, for the catalysts with a higher cobalt loading  
363 (35Co/Al<sub>2</sub>O<sub>3</sub> and 40Co/Al<sub>2</sub>O<sub>3</sub>) the main signal (780.1–780.2 eV) was closer to that of the  
364 bulk Co<sub>3</sub>O<sub>4</sub> (780.1 eV). This indicated that Co<sub>3</sub>O<sub>4</sub> was the most abundant phase on the  
365 surface [49].

#### 366 FIGURE 6

367 The redox properties were investigated by temperature-programmed reduction with  
368 hydrogen. The resulting profiles are included in Figure 7. It is worth pointing out that all  
369 cobalt species present in the catalysts were completely reduced to metallic Co. This was  
370 verified by XRD analysis of the samples recovered after the TPR run since only metallic  
371 Co and Al<sub>2</sub>O<sub>3</sub> were detected (Figure S5, Supplementary material). Two main H<sub>2</sub> uptakes  
372 were clearly distinguished. The first contribution, located at about 250–450 °C, could be  
373 assigned to reduction of free Co<sub>3</sub>O<sub>4</sub>. This consumption could be in turn subdivided into  
374 other two with peak reduction temperatures at 310 and 380–440 °C, following the same  
375 reduction steps as for the bulk Co<sub>3</sub>O<sub>4</sub> catalysts. Note that, unlike the bulk CC sample, the  
376 sequential reduction  $\text{Co}^{3+} \rightarrow \text{Co}^{2+} \rightarrow \text{Co}^0$  was less discernible. The second main uptake,  
377 centred at higher temperatures (660–730 °C), could be related to Co species with a  
378 substantially lower reducibility. In the literature there is still a debate on the nature of this  
379 contribution since it could be attributed to either the formation of cobalt aluminate  
380 CoAl<sub>2</sub>O<sub>4</sub> [46,50], or to strong interactions between Co species and the alumina support  
381 [26,51]. In an attempt to shed some light on the origin of this contribution, a H<sub>2</sub>-TPR  
382 analysis of the bulk cobalt aluminate calcined at 600 °C was performed in order to serve

383 as a reference for comparison with the supported catalysts. Its corresponding profile  
384 included in Figure 7 was similar to those of the alumina supported catalysts. Thus, a low  
385 H<sub>2</sub> consumption was noticed at about 450 °C, which corresponded to the reduction of  
386 cobalt species (probably Co<sub>3</sub>O<sub>4</sub>) not fully incorporated into the lattice of CoAl<sub>2</sub>O<sub>4</sub>. Above  
387 600 °C the full reduction of CoAl<sub>2</sub>O<sub>4</sub> took place. Accordingly, the measured overall H<sub>2</sub>  
388 uptake (6.49 mmol H<sub>2</sub> g<sup>-1</sup>) was slightly higher than the theoretical value for pure CoAl<sub>2</sub>O<sub>4</sub>  
389 (5.65 mmol H<sub>2</sub> g<sup>-1</sup>). Therefore, the comparison between the profiles of the alumina  
390 supported catalysts and that of the bulk CoAl<sub>2</sub>O<sub>4</sub> sample evidenced that the high-  
391 temperature H<sub>2</sub> consumption observed on the supported Co<sub>3</sub>O<sub>4</sub> samples could be assigned  
392 to the presence of varying amounts of cobalt aluminate. Note that the shoulder at about  
393 900 °C observed in the profile of the 20Co/Al<sub>2</sub>O<sub>3</sub> catalyst was due to an instrumental  
394 artifact involving the application of the heating ramp of the experiment. Occasionally,  
395 when the temperature were close (about 10 °C lower) to the temperature limit of the run  
396 (in this case, 900 °C), the furnace would stop heating. Then the ongoing reduction process  
397 underwent a sudden halt that resulted in that small sharp peak, which had no meaning on  
398 the redox properties of the sample.

399 The quantitative integration of the profiles (Table 3) revealed that the overall H<sub>2</sub> uptake  
400 of the 10Co/Al<sub>2</sub>O<sub>3</sub> and 20Co/Al<sub>2</sub>O<sub>3</sub> catalysts was very close to that expected when  
401 assuming that all cobalt species were present as CoAl<sub>2</sub>O<sub>4</sub>. By contrast, the observed  
402 uptake for the 35Co/Al<sub>2</sub>O<sub>3</sub> and 40Co/Al<sub>2</sub>O<sub>3</sub> samples was comparable with that  
403 theoretically predicted for the exclusive presence of Co<sub>3</sub>O<sub>4</sub>. Based on the corresponding  
404 H<sub>2</sub> consumption at 250–450 °C and 600–800 °C the relative distribution of Co species  
405 between Co<sub>3</sub>O<sub>4</sub> and CoAl<sub>2</sub>O<sub>4</sub> could be estimated for each sample. It was found that cobalt  
406 aluminate was the principal phase over the catalyst with the lowest loading (10Co/Al<sub>2</sub>O<sub>3</sub>).  
407 When increasing the metal content up to 20wt% the amount of both species increased. It

408 therefore seemed that the previously formed  $\text{CoAl}_2\text{O}_4$  layer grew. However, above this  
409 Co concentration (30Co/ $\text{Al}_2\text{O}_3$ , 35Co/ $\text{Al}_2\text{O}_3$  and 40Co/ $\text{Al}_2\text{O}_3$  samples) the amount of  
410 metal as  $\text{CoAl}_2\text{O}_4$  remained constant around 13-14wt.%, irrespective of the cobalt  
411 loading. It could be then reasonably believed that the formed  $\text{Co}_3\text{O}_4$  crystallites were  
412 located on top of this aluminate layer, and in principle, did not further converted into  
413 aluminate. This assumption was coherent with the larger  $\text{H}_2$  uptake required for the  
414 reduction of free  $\text{Co}_3\text{O}_4$  over these samples.

#### 415 FIGURE 7

416

#### 417 3.3. Characterisation of Ce-doped $\text{Co}_3\text{O}_4$ bulk catalysts

418 The textural and structural properties of the bulk Ce-doped  $\text{Co}_3\text{O}_4$  ( $x\text{Ce}/\text{Co}_3\text{O}_4$ ) samples  
419 along with the CC sample and pure  $\text{CeO}_2$  (for reference) are shown in Table 4. The  
420 specific surface area of Ce-doped catalysts varied between 30 and 35  $\text{m}^2 \text{g}^{-1}$ , which was  
421 more than twice that of the surface area of the CC sample, while the pore volume  
422 increased by 50% approximately and the pore diameter decreased by the same amount,  
423 thus demonstrating that the addition of Ce to the bulk  $\text{Co}_3\text{O}_4$  could improve their textural  
424 properties.

#### 425 TABLE 4

426 The  $x\text{Ce}/\text{Co}_3\text{O}_4$  samples showed the various diffraction signals of the cubic  $\text{Co}_3\text{O}_4$  but  
427 slightly shifted from their positions with respect to the pure spinel (Figure 8). In addition,  
428 the crystallite size significantly decreased from 63 to 29–38 nm. On the other hand, the  
429 samples with a Ce loading of 15 and 20wt% also exhibited signals ( $2\theta = 28.8^\circ, 33.3^\circ,$   
430  $47.7^\circ, 56.6^\circ, 59.4^\circ, 69.6^\circ, 76.9^\circ$  and  $79.3^\circ$ ) related to segregated cubic fluorite-like  $\text{CeO}_2$   
431 (JCPDS 00-034-0394). These evidences pointed out that the addition of Ce caused a  
432 distortion in the spinel structure, which in turn decreased the  $\text{Co}_3\text{O}_4$  crystallite size and

433 increased the unit cell size, but only for the Ce loadings of 5 and 10% wt., as can be seen  
434 in Figure S6 (Supplementary material). These effects have also been reported by other  
435 authors [52,53], with the latter being attributed to the larger ionic radius of  $\text{Ce}^{4+}$  (101 pm)  
436 in comparison with  $\text{Co}^{2+}$  (79 pm) and  $\text{Co}^{3+}$  (69 pm). The upper limit for the amount of  
437 cerium atoms that could be inserted into the lattice of  $\text{Co}_3\text{O}_4$  seemed to be close to 10% wt.  
438 Above this loading, excess of cerium led to the formation of segregated  $\text{CeO}_2$ .

#### 439 FIGURE 8

440 To further assess the distortion caused by the insertion of Ce atoms into the lattice of the  
441  $\text{Co}_3\text{O}_4$  spinel, Raman spectrometry was applied to all Ce-doped samples. The resulting  
442 spectra are included in Figure 9. The doped oxides displayed the same five Raman bands  
443 also observed for the pure  $\text{Co}_3\text{O}_4$ , but shifted from their original positions and with  
444 broader shapes, thus suggesting the distortion of the  $\text{Co}_3\text{O}_4$  lattice. Hence, the bands  
445 located at 194, 519 and 617  $\text{cm}^{-1}$  could be assigned to the  $\text{F}_{2g}$  mode, while the bands at  
446 479 and 687  $\text{cm}^{-1}$  could be assigned to the  $\text{E}_g$  and  $\text{A}_{1g}$  modes, respectively [13]. Pure  
447  $\text{CeO}_2$ , however, only displayed a markedly intense signal, located at 462  $\text{cm}^{-1}$ , attributable  
448 to the symmetrical stretching of  $\text{CeO}_8$  units [54]. The  $x\text{Ce}/\text{Co}_3\text{O}_4$  samples also exhibited  
449 much weaker forms of this signal, also shifted from its original position. This pointed out  
450 that the segregated  $\text{CeO}_2$  in the 15Ce/ $\text{Co}_3\text{O}_4$  and 20Ce/ $\text{Co}_3\text{O}_4$  samples could also present  
451 some degree of distortion on its own lattice. The band related to the  $\text{A}_{1g}$  mode showed a  
452 much broader shape for the Ce-doped samples, with relatively higher FWHM values  
453 between 17 and 27  $\text{cm}^{-1}$  in comparison with the pure cobalt oxide (11  $\text{cm}^{-1}$ ). The highest  
454 values were noted over the samples 5Ce/ $\text{Co}_3\text{O}_4$  and 10Ce/ $\text{Co}_3\text{O}_4$ , thereby pointing out that  
455 the largest extent of lattice distortion occurred in these catalysts. Accordingly, these were  
456 the samples that presented the largest cell size.

#### 457 FIGURE 9

458 The XPS analysis of Ce-doped samples also helped in determining the role of Ce and its  
459 eventual influence on the valence changes of cobalt species. The spectra of all  $x\text{Ce}/\text{Co}_3\text{O}_4$   
460 samples were fitted with ten peaks corresponding to five pairs of spin-orbit doublets.  
461 Following the convention adopted by Romeo et al. [55], letters U and V were used to  
462 refer to the  $3d_{5/2}$  and  $3d_{3/2}$  spin-orbit components, respectively. From the five pairs of  
463 peaks, three of them (namely V,U; V'',U'' and V''',U''') were associated with electrons  
464 from  $\text{Ce}^{4+}$  while the remaining pairs ( $V_0,U_0$  and V',U') were attributed to electrons from  
465  $\text{Ce}^{3+}$  species. As an example, the fitted Ce3d spectrum of the  $10\text{Ce}/\text{Co}_3\text{O}_4$  sample is  
466 shown in Figure S7 (Supplementary material).

467 The  $\text{Ce}^{3+}/\text{Ce}^{4+}$  molar ratios were obtained from the areas of both  $3d_{5/2}$  and  $3d_{3/2}$   
468 components for each species. These calculated ratios were correlated with the molar  
469  $\text{Co}^{3+}/\text{Co}^{2+}$  ratios calculated from the respective Co2p spectra, as shown in Figure 10. An  
470 inverse relationship was found, which could be explained in terms of the equilibrium  $\text{Ce}^{3+}$   
471  $+ \text{Co}^{3+} \leftrightarrow \text{Ce}^{4+} + \text{Co}^{2+}$ , established by the requirement of charge balance within the cations  
472 of the spinel lattice [56,57]. An increase in  $\text{Co}^{3+}$  population at the cost of  $\text{Co}^{2+}$  resulted in  
473 a decrease of  $\text{Ce}^{3+}$  ions in favour of  $\text{Ce}^{4+}$ .

#### 474 FIGURE 10

475 The redox properties of the Ce-doped catalysts were investigated by temperature-  
476 programmed reduction with hydrogen ( $\text{H}_2$ -TPR) and temperature-programmed reaction  
477 with methane ( $\text{CH}_4$ -TPRe). The corresponding  $\text{H}_2$ -TPR profiles are included in Figure 11.  
478 The hydrogen consumption profiles of the  $x\text{Ce}/\text{Co}_3\text{O}_4$  catalysts were similar to those  
479 displayed by the bulk  $\text{Co}_3\text{O}_4$ , showing the same two-step reduction process, with peak  
480 temperatures at 310 and 375 °C. Note that the second reduction peak, assigned to the  
481 reduction of  $\text{Co}^{2+}$  ions, was characterised by a broader temperature window with respect  
482 to the pure cobalt oxide, probably due to the distortion caused by the insertion of Ce atoms

483 into the spinel lattice. The reduction profile of CeO<sub>2</sub> also exhibited a two-step reduction  
484 process, where the first step, centred at about 320 °C, is usually attributed to the reduction  
485 of the surface while the second one, located at 735 °C, is assigned to the reduction of the  
486 bulk [58]. However, the intensity of these reduction events was substantially lower than  
487 for the reduction of Co<sub>3</sub>O<sub>4</sub>, and none of the Ce-doped catalysts revealed signals of CeO<sub>2</sub>  
488 reduction in their TPR profiles, presumably owing to the low amount of free CeO<sub>2</sub> present  
489 in the samples. The results included in Table 5 pointed out that Ce doping did not result  
490 in a relevant variation of the relative H<sub>2</sub> uptake at low and high temperature corresponding  
491 to the reduction of the spinel.

492 FIGURE 11

493 TABLE 5

494 Since the investigation of the redox properties of the xCe/Co<sub>3</sub>O<sub>4</sub> oxides by H<sub>2</sub>-TPR did  
495 not evidence marked differences among the various samples, a new attempt was made by  
496 substituting H<sub>2</sub> by CH<sub>4</sub>. This change could provide more useful insights on the  
497 characterisation and identification of the available oxygen species for methane oxidation.  
498 The exit stream of the CH<sub>4</sub>-TPRe experiment was analysed by mass spectrometry. Thus,  
499 the m/z = 44 (CO<sub>2</sub>) and the m/z = 28 (CO) signals were monitored. The evolution of these  
500 two species with the temperature for all xCe/Co<sub>3</sub>O<sub>4</sub> catalysts and the CC sample are  
501 shown in Figure 12.

502 FIGURE 12

503 Over all samples the formation of CO<sub>2</sub> occurred at 350–550 °C and 600–700 °C. At lower  
504 temperatures the generation was assigned to the oxidation of methane by oxygen species  
505 associated with Co<sup>3+</sup> ions. At higher temperatures the CO<sub>2</sub> production was attributed to  
506 the oxidation of methane by oxygen species associated with Co<sup>2+</sup> ions [59]. However, as  
507 opposed to the H<sub>2</sub>-TPR profiles, the temperature windows for both reactions were clearly

508 discernible. In all cases, the formation of CO<sub>2</sub> at high temperatures was also accompanied  
509 by the generation of CO and H<sub>2</sub> to some extent. This could be due to the ability of Co<sup>2+</sup>  
510 ions to catalyse the reforming of methane as well [60] and also due to the deficit of oxygen  
511 present in the catalysts after all Co<sup>3+</sup> ions were reduced. Both CO<sub>2</sub> contributions took the  
512 shape of definite non-Gaussian peaks. Interestingly, for the 10Ce/Co<sub>3</sub>O<sub>4</sub> sample, the  
513 formation of CO<sub>2</sub> occurred at significantly lower temperatures (460 and 605 °C) when  
514 compared with the CC sample (485 and 620 °C). Each CH<sub>4</sub>-TPRe experiment was  
515 followed by a H<sub>2</sub>-TPR analysis to check if methane could completely reduce the catalysts.  
516 No hydrogen uptake was found, thereby evidencing that all samples were completely  
517 reduced by methane. Integration and quantification of the CO<sub>2</sub> production at low and high  
518 temperatures (Table 5) revealed a better behaviour for the conversion of CH<sub>4</sub> at low  
519 temperatures over the 10Ce/Co<sub>3</sub>O<sub>4</sub> sample. These results demonstrated that the addition  
520 of small amounts of Ce to bulk Co<sub>3</sub>O<sub>4</sub> catalysts improved their ability for methane  
521 oxidation.

522

#### 523 3.4. Comparison between Co<sub>3</sub>O<sub>4</sub>/Al<sub>2</sub>O<sub>3</sub> and Ce-doped Co<sub>3</sub>O<sub>4</sub> bulk catalysts

524 Catalytic activity of alumina supported and Ce-doped Co<sub>3</sub>O<sub>4</sub> catalysts were examined  
525 under the same conditions as for the bulk Co<sub>3</sub>O<sub>4</sub> catalysts. The corresponding light-off  
526 curves are included in Figure 13. It was noticed that the activity of the alumina supported  
527 samples expectedly increased with Co loading, with a T<sub>50</sub> value of 515 and 510 °C over  
528 the 35Co/Al<sub>2</sub>O<sub>3</sub> and 40Co/Al<sub>2</sub>O<sub>3</sub> catalysts, respectively. Nevertheless, in no case their  
529 activity was higher than that of the bulk catalysts, despite exhibiting much better textural  
530 properties. This was probably due to two reasons. First, cobalt aluminate, hardly reducible  
531 at the selected reaction temperatures, fixed a great amount of the cobalt deposited, thereby  
532 decreasing the availability of potentially active cobalt species. Recall that the activity of

533 pure  $\text{CoAl}_2\text{O}_4$  was negligible. Secondly, as shown by the  $\text{H}_2$ -TPR profiles, the amount of  
534 easily reducible, highly active  $\text{Co}^{3+}$  in the supported catalysts was lower than that of bulk  
535 catalysts, which made free  $\text{Co}_3\text{O}_4$  within the support less active than the bulk  $\text{Co}_3\text{O}_4$ .  
536 Similar results were obtained by other authors, for  $\text{Co}_3\text{O}_4/\text{Al}_2\text{O}_3$  catalysts obtained by  
537 both wet [11] and incipient wetness impregnation [26].

538

### FIGURE 13

539 The reaction rate estimated under differential conditions ( $X < 20\%$  at  $425\text{ }^\circ\text{C}$ ) are listed in  
540 Table 2. The highest reaction rate was found over the  $35\text{Co}/\text{Al}_2\text{O}_3$  catalyst ( $2.2\text{ mmol CH}_4$   
541  $\text{g}_{\text{Co}}^{-1}\text{ h}^{-1}$ ) followed by the  $40\text{Co}/\text{Al}_2\text{O}_3$  and  $30\text{Co}/\text{Al}_2\text{O}_3$  samples ( $2.1$  and  $1.9\text{ mmol CH}_4$   
542  $\text{g}_{\text{Co}}^{-1}\text{ h}^{-1}$ , respectively). By contrast, both  $10\text{Co}/\text{Al}_2\text{O}_3$  and  $20\text{Co}/\text{Al}_2\text{O}_3$  samples showed a  
543 noticeably lower reaction rate, around  $1.2\text{ mmol CH}_4\text{ g}_{\text{Co}}^{-1}\text{ h}^{-1}$ . On the other hand, a  
544 progressive decrease in the apparent activation energy with Co loading was evident. Over  
545 the catalysts with a low Co content, where  $\text{CoAl}_2\text{O}_4$  was the most abundant phase, the  
546 activation energy was around  $100\text{ kJ mol}^{-1}$ . For higher loadings, and more particularly  
547 over the  $35\text{Co}/\text{Al}_2\text{O}_3$  and  $40\text{Co}/\text{Al}_2\text{O}_3$  catalysts, the activation energy was close ( $78$ – $79$   
548  $\text{kJ mol}^{-1}$ ) to that observed for the bulk  $\text{Co}_3\text{O}_4$  catalyst (CC sample). These values were  
549 evaluated from the fit of experimental conversion data to the Equation 1.

550 Regarding Ce-doped samples all the light-off curves were relatively similar with a  $T_{50}$  in  
551 the  $425$ – $435\text{ }^\circ\text{C}$  range. It must be pointed out that the pure  $\text{CeO}_2$  was virtually inactive,  
552 with a conversion as low as  $10\%$  at  $600\text{ }^\circ\text{C}$ . Only the  $10\text{Ce}/\text{Co}_3\text{O}_4$  sample showed a  
553 slightly better behaviour with respect to the pure bulk  $\text{Co}_3\text{O}_4$  catalyst. More perceptible  
554 differences were noticed when the specific reaction rates at  $375\text{ }^\circ\text{C}$  ( $X < 20\%$ ) were  
555 compared. Thus, it was  $2\text{ mmol CH}_4\text{ g}_{\text{Co}}^{-1}\text{ h}^{-1}$  over the  $10\text{Ce}/\text{Co}_3\text{O}_4$  sample and  $1.8\text{ mmol}$   
556  $\text{CH}_4\text{ g}_{\text{Co}}^{-1}\text{ h}^{-1}$  over the pure cobalt oxide. This revealed that the addition of cerium had a  
557 positive effect on the specific activity of bulk  $\text{Co}_3\text{O}_4$ . It is worth pointing out that the

558 alumina supported catalysts required temperatures at least 50 °C higher to achieve similar  
559 reaction rates. The estimated apparent activation energy of the 5Ce/Co<sub>3</sub>O<sub>4</sub>, 10Ce/Co<sub>3</sub>O<sub>4</sub>  
560 and 15Ce/Co<sub>3</sub>O<sub>4</sub> catalysts were 78–79 kJ mol<sup>-1</sup>, close to the value determined for the pure  
561 counterpart. Over the 20Ce/Co<sub>3</sub>O<sub>4</sub> catalyst, characterised by a considerable amount of  
562 segregated ceria, the value significantly increased up to 85 kJ mol<sup>-1</sup>. Note that pure CeO<sub>2</sub>  
563 gave an activation energy of 108 kJ mol<sup>-1</sup>. The relationship shown in Figure 14 revealed  
564 that the specific reaction rate was clearly influenced by the mobility of the oxygen species,  
565 which was evaluated from the amount of oxygen reacting with methane at low  
566 temperatures, which corresponded to the Co<sup>3+</sup> → Co<sup>2+</sup> reduction step in the CH<sub>4</sub>-TPRe  
567 run. In sum, it could be concluded that the addition of small amounts of cerium atoms,  
568 which were introduced into the lattice of Co<sub>3</sub>O<sub>4</sub>, resulted in an enhancement of the  
569 intrinsic activity of the spinel owing to a distortion of the crystalline structure which  
570 ultimately led to an increased population of Co<sup>3+</sup>, an improved reducibility and a higher  
571 mobility of the oxygen species in the spinel lattice.

572 **FIGURE 14**

573 The deep oxidation of methane over Ce-Co oxide catalysts has been widely investigated  
574 in the recent years. For example, Li et al. achieved a T<sub>50</sub> of 400 °C (25 °C lower than in  
575 this work) under similar reaction conditions over a Ce-Co catalyst prepared by a sol-gel  
576 method [28]. Vickers et al. obtained comparable results (T<sub>50</sub> around 400 °C) using CeO<sub>2</sub>  
577 supported over a meso-Co<sub>3</sub>O<sub>4</sub> obtained using KIT-6 as hard template but operating at  
578 180 mL CH<sub>4</sub> g<sup>-1</sup> h<sup>-1</sup> [61]. In both cases, the Ce/Co molar ratio (0.33 and 0.10, respectively)  
579 used was significantly higher than in this work (0.06), which points out that the activity  
580 promoting effect of cerium in those catalysts was actually lower than that observed in this  
581 work. In addition, Liotta et al. [62] achieved a T<sub>50</sub> of 455 °C (180 mL CH<sub>4</sub> g<sup>-1</sup> h<sup>-1</sup>) by  
582 using Co<sub>3</sub>O<sub>4</sub> supported over CeO<sub>2</sub> with a Ce/Co molar ratio of 1.1. Our results therefore

583 evidenced that active Ce-Co catalysts could be designed with a relatively low Ce content.  
584 Finally, attention was also paid to examining the stability of the most active catalysts,  
585 namely 10Ce/Co<sub>3</sub>O<sub>4</sub> and CC samples, when operating at constant temperature (450 °C)  
586 during a relatively prolonged time (150 hours). The results included in Figure S8  
587 (Supplementary material) revealed that both oxides gave a relatively stable conversion  
588 close to 75%, although the cerium-free sample showed a slight instability. The  
589 characterisation of the used 10Ce/Co<sub>3</sub>O<sub>4</sub> sample by BET measurements and XRD  
590 revealed a reduced impact on its surface area (30 m<sup>2</sup> g<sup>-1</sup>, 35 m<sup>2</sup> g<sup>-1</sup> for the fresh sample)  
591 and crystallite size (30 nm, 29 nm for the fresh sample).  
592 Given the reasonably good results achieved by the 10Ce/Co<sub>3</sub>O<sub>4</sub> catalyst its stability at  
593 425 °C was also evaluated under humid conditions (in the presence of 5% H<sub>2</sub>O) for 150  
594 hours. The results are also shown in Figure S8 (Supplementary material). It was found  
595 that water noticeably decreased the catalytic performance with a reasonably constant  
596 conversion around 40%. The surface area after this run decreased to 24 m<sup>2</sup> g<sup>-1</sup> in line with  
597 the concomitant enlargement of the crystallite size (35 nm). This used sample was further  
598 submitted to an additional stability test under dry conditions for 20 hours (Figure S8,  
599 Supplementary material). It was noticed that conversion was not fully recovered, but it  
600 was still around 65%. This finding certainly evidenced that water, apart from inhibiting  
601 the catalytic activity by competitive effects, also had a significant negative effect on the  
602 physicochemical properties of the sample [17,63].

603

#### 604 **4. Conclusions**

605 The performance of three type of Co<sub>3</sub>O<sub>4</sub> catalysts, namely bulk, alumina-supported and  
606 Ce-doped samples, was examined for the combustion of methane under similar reaction  
607 conditions to those in the exhaust gas of VNG engines. The activity of bulk catalysts was

608 found to be controlled by an increased  $\text{Co}^{3+}/\text{Co}^{2+}$  molar ratio that in turn evidenced a more  
609 active role of surface lattice oxygen in the reaction. Higher reaction rates were achieved  
610 by  $\text{Co}_3\text{O}_4$  catalysts prepared by basic aqueous precipitation. Interestingly, the addition of  
611 a relatively small amount of cerium (10% wt.) to the  $\text{Co}_3\text{O}_4$  lattice led to an increase in  
612 the inherent catalytic activity of the cobalt phase due to an improvement in the mobility  
613 of lattice oxygen species associated with easily reducible  $\text{Co}^{3+}$  ions. This optimised  
614 catalyst exhibited a marked stability under both dry and humid conditions during a  
615 relatively prolonged reaction time. On the other hand, owing to the notable negative  
616 impact induced by cobalt aluminate formation, the behaviour of alumina supported  
617 catalysts was shown to be inferior with respect to the bulk samples. As a result, notable  
618 conversion levels were only attained with a Co loading higher than 30% wt.

619

## 620 **Acknowledgements**

621 The author wish to thank the financial support provided by the Ministry of Economy and  
622 Competitiveness (CTQ2016-80253-R), Basque Government (IT657-13) and the  
623 University of the Basque Country UPV/EHU, and the technical and human support  
624 provided by SGIker (UPV/EHU) and the University of Cádiz.

625

## 626 **Appendix A. Supplementary data**

627 Supplementary data associated with this article can be found in the online version.

628

## 629 **References**

- 630 [1] M.I. Jahirul, H.H. Masjuki, R. Saidur, M.A. Kalam, M.H. Jayed, M.A. Wazed,  
631 Appl. Therm. Eng. 30 (2010) 2219-2226.
- 632 [2] M. Hussain, F.A. Deorsola, N. Russo, D. Fino, R. Pirone, Fuel 149 (2015) 2-7.
- 633 [3] S. Di Pascoli, A. Femia, T. Luzzati, Ecol. Econ. 38 (2001) 179-189.

- 634 [4] T. Korakianitis, A.M. Namasivayam, R.J. Crookes, *Prog. Energ. Combust.* 37  
635 (2011) 89-112.
- 636 [5] Z. Li, G.B. Hoflund, *J. Nat. Gas Chem.* 12 (2003) 153-160.
- 637 [6] J.K. Lampert, M.S. Kazi, R.J. Farrauto, *Appl. Catal. B Environ.* 14 (1997) 211-  
638 223.
- 639 [7] Q. Xu, K.C. Kharas, B.J. Croley, A.K. Datye, *ChemCatChem* 3 (2011) 1004-  
640 1014.
- 641 [8] L.S. Escandón, D. Niño, E. Díaz, S. Ordóñez, F.V. Díez, *Catal. Commun.* 9 (2008)  
642 2291-2296.
- 643 [9] S. Ordóñez, J.R. Paredes, F.V. Díez, *Appl. Catal. A Gen.* 341 (2008) 174-180.
- 644 [10] A. Setiawan, E.M. Kennedy, B.Z. Dlugogorski, A.A. Adesina, M. Stockenhuber,  
645 *Catal. Today* 258 (2015) 276-283.
- 646 [11] T. Xiao, S. Ji, H. Wang, K.S. Coleman, M.L.H. Green, *J. Mol. Catal. A Chem.*  
647 175 (2001) 111-123.
- 648 [12] J. Chen, H. Arandiyán, X. Gao, J. Li, *Catal. Surv. Asia* 19 (2015) 140-171.
- 649 [13] Q. Liu, L. Wang, M. Chen, Y. Cao, H. He, K. Fan, *J. Catal.* 263 (2009) 104-113.
- 650 [14] G. Salek, P. Alphonse, P. Dufour, S. Guillemet-Fritsch, C. Tenailleau, *Appl.*  
651 *Catal. B Environ.* 147 (2014) 1-7.
- 652 [15] Q. Ren, S. Mo, R. Peng, Z. Feng, M. Zhang, L. Chen, M. Fu, J. Wu, D. Ye, J.  
653 *Mater. Chem. A* 6 (2018) 498-509.
- 654 [16] J. González-Prior, R. López-Fonseca, J.I. Gutiérrez-Ortiz, B. de Rivas, *Appl.*  
655 *Catal. B Environ.* 222 (2018) 9-17.
- 656 [17] L.F. Liotta, G. Di Carlo, G. Pantaleo, A.M. Venezia, G. Deganello, *Appl. Catal.*  
657 *B Environ.* 66 (2006) 217-227.
- 658 [18] N. Bahlawane, *Appl. Catal. B Environ.* 67 (2006) 168-176.
- 659 [19] Y. Ji, Z. Zhao, A. Duan, G. Jiang, J. Liu, *J. Phys. Chem. C* 113 (2009) 7186-7199.
- 660 [20] N. Bahlawane, P.H.T. Ngamou, V. Vannier, T. Kottke, J. Heberle, K. Kohse-  
661 Höinghaus, *Phys. Chem. Chem. Phys.* 11 (2009) 9224-9232.
- 662 [21] Z. Tian, P.H. Tchoua Ngamou, V. Vannier, K. Kohse-Höinghaus, N. Bahlawane,  
663 *Appl. Catal. B Environ.* 117-118 (2012) 125-134.
- 664 [22] N. van Vegten, T. Baidya, F. Krumeich, W. Kleist, A. Baiker, *Appl. Catal. B*  
665 *Environ.* 97 (2010) 398-406.

- 666 [23] Z. Chen, S. Wang, W. Liu, X. Gao, D. Gao, M. Wang, S. Wang, *Appl. Catal. A*  
667 *Gen.* 525 (2016) 94-102.
- 668 [24] Z. Pu, H. Zhou, Y. Zheng, W. Huang, X. Li, *Appl. Surf. Sci.* 410 (2017) 14-21.
- 669 [25] U. Zavyalova, P. Scholz, B. Ondruschka, *Appl. Catal. A Gen.* 323 (2007) 226-  
670 233.
- 671 [26] Q. Wang, Y. Peng, J. Fu, G.Z. Kyzas, S.M.R. Billah, S. An, *Appl. Catal. B*  
672 *Environ.* 168-169 (2015) 42-50.
- 673 [27] N.E. Machin, C. Karakaya, A. Celepci, *Energ. Fuel.* 22 (2008) 2166-2171.
- 674 [28] H. Li, G. Lu, D. Qiao, Y. Wang, Y. Guo, Y. Guo, *Catal. Lett.* 141 (2011) 452-  
675 458.
- 676 [29] M. Kumar, G. Rattan, R. Prasad, *Can. Chem. Trans.* 3 (2015) 381-409.
- 677 [30] B. De Rivas, R. López-Fonseca, C. Jiménez-González, J.I. Gutiérrez-Ortiz, *J.*  
678 *Catal.* 281 (2011) 88-97.
- 679 [31] A.A. Mirzaei, H.R. Shaterian, R.W. Joyner, M. Stockenhuber, S.H. Taylor, G.J.  
680 Hutchings, *Catal. Commun.* 4 (2003) 17-20.
- 681 [32] Eurokin. <http://eurokin.org/>, 2018 (accessed 20 February 2018).
- 682 [33] A. Aranzabal, J.A. González-Marcos, J.L. Ayastuy, J.R. González-Velasco,  
683 *Chem. Eng. Sci.* 61 (2006) 3564-3576.
- 684 [34] C. Shi, Y. Wang, A. Zhu, B. Chen, C. Au, *Catal. Commun.* 28 (2012) 18-22.
- 685 [35] A. Biabani-Ravandi, M. Rezaei, *Chem. Eng. J.* 184 (2012) 141-146.
- 686 [36] S. Arnone, G. Bagnasco, G. Busca, L. Lisi, G. Russo, M. Turco, *Stud. Surf. Sci.*  
687 *Catal.* 119 (1998) 65-70.
- 688 [37] J. González-Prior, R. López-Fonseca, J.I. Gutiérrez-Ortiz, B. de Rivas, *Appl.*  
689 *Catal. B Environ.* 199 (2016) 384-393.
- 690 [38] S.A. Singh, G. Madras, *Appl. Catal. A Gen.* 504 (2015) 463-475.
- 691 [39] M.C. Biesinger, B.P. Payne, A.P. Grosvenor, L.W.M. Lau, A.R. Gerson, R.S.C.  
692 Smart, *Appl. Surf. Sci.* 257 (2011) 2717-2730.
- 693 [40] J. Dupin, D. Gonbeau, P. Vinatier, A. Levasseur, *Phys. Chem. Chem. Phys.* 2  
694 (2000) 1319-1324.
- 695 [41] P. Stefanov, S. Todorova, A. Naydenov, B. Tzaneva, H. Kolev, G. Atanasova, D.  
696 Stoyanova, Y. Karakirova, K. Aleksieva, *Chem. Eng. J.* 266 (2015) 329-338.

- 697 [42] G.I. Golodets, Chapter V: The Kinetics of Gas-Phase Heterogeneous Catalytic  
698 Reactions Involving Molecular Oxygen, in: G.I. Golodets (Ed.), Heterogeneous  
699 Catalytic Reactions Involving Molecular Oxygen, Elsevier, Amsterdam, 1983, pp.  
700 126-150.
- 701 [43] J.R. Paredes, E. Díaz, F.V. Díez, S. Ordóñez, *Energ. Fuel.* 23 (2009) 86-93.
- 702 [44] J. Li, X. Liang, S. Xu, J. Hao, *Appl. Catal. B Environ.* 90 (2009) 307-312.
- 703 [45] Y. Brik, M. Kacimi, M. Ziyad, F. Bozon-Verduraz, *J. Catal.* 202 (2001) 118-128.
- 704 [46] L.G.A. van de Water, G.L. Bezemer, J.A. Bergwerff, M. Versluijs-Helder, B.M.  
705 Weckhuysen, K.P. de Jong, *J. Catal.* 242 (2006) 287-298.
- 706 [47] T. Das, S. Sengupta, G. Deo, *React. Kinet. Mech. Catal.* 110 (2013) 147-162.
- 707 [48] F. Dumond, E. Marceau, M. Che, *J. Phys. Chem. C* 111 (2007) 4780-4789.
- 708 [49] X. Duan, M. Pan, F. Yu, D. Yuan, *J. Alloy. Compd.* 509 (2011) 1079-1083.
- 709 [50] I. Zacharaki, C.G. Kontoyannis, S. Boghosian, A. Lycourghiotis, C. Kordulis,  
710 *Catal. Today* 143 (2009) 38-44.
- 711 [51] B. Solsona, T.E. Davies, T. Garcia, I. Vázquez, A. Dejoz, S.H. Taylor, *Appl.*  
712 *Catal. B Environ.* 84 (2008) 176-184.
- 713 [52] D. Li, L. Wang, M. Koike, Y. Nakagawa, K. Tomishige, *Appl. Catal. B Environ.*  
714 102 (2011) 528-538.
- 715 [53] G. Zou, Y. Xu, S. Wang, M. Chen, W. Shangguan, *Catal. Sci. Technolog.* 5 (2015)  
716 1084-1092.
- 717 [54] K.K. Babitha, A. Sreedevi, K.P. Priyanka, B. Sabu, T. Varghese, *Indian J. Pure*  
718 *Appl. Phys.* 53 (2015) 596-603.
- 719 [55] M. Romeo, K. Bak, J. El Fallah, F. Le Normand, L. Hilaire, *Surf. Interface Anal.*  
720 20 (1993) 508-512.
- 721 [56] J. Chen, C. Li, S. Li, P. Lu, L. Gao, X. Du, Y. Yi, *Chem. Eng. J.* 338 (2018) 358-  
722 368.
- 723 [57] R. Dziembaj, A. Chojnacka, Z. Piwowska, M. Gajewska, M. Swietoslowski, S.  
724 Górecka, M. Molenda, *Catal Today* (2018) 'in press'.
- 725 [58] M. Florea, F. Matei-Rutkovska, G. Postole, A. Urda, F. Neatu, V.I. Pârvulescu, P.  
726 Gelin, *Catal. Today* 306 (2018) 166-171.
- 727 [59] L. Hu, Q. Peng, Y. Li, *J. Am. Chem. Soc.* 130 (2008) 16136-16137.

- 728 [60] A.W. Budiman, S. Song, T. Chang, C. Shin, M. Choi, *Catal. Surv. Asia* 16 (2012)  
729 183-197.
- 730 [61] S.M. Vickers, R. Gholami, K.J. Smith, M.J. MacLachlan, *ACS Appl. Mater. Inter.*  
731 7 (2015) 11460-11466.
- 732 [62] L.F. Liotta, G. Di Carlo, G. Pantaleo, G. Deganello, *Appl. Catal. B Environ.* 70  
733 (2007) 314-322.
- 734 [63] D. Qiao, G. Lu, Y. Guo, Y. Wang, Y. Guo, *J. Rare Earth.* 28 (2010) 742-746.
- 735

736 **CAPTIONS FOR TABLES AND FIGURES**

- 737 Table 1. Physicochemical characterisation of bulk  $\text{Co}_3\text{O}_4$  catalysts.
- 738 Table 2. Kinetic results of all cobalt catalysts.
- 739 Table 3. Physicochemical characterisation of  $x\text{Co}/\text{Al}_2\text{O}_3$  catalysts.
- 740 Table 4. Textural and structural properties of  $x\text{Ce}/\text{Co}_3\text{O}_4$  catalysts.
- 741 Table 5. Results of  $\text{H}_2$ -TPR and  $\text{CH}_4$ -TPRe analysis of the  $x\text{Ce}/\text{Co}_3\text{O}_4$  catalysts.
- 742
- 743 Figure 1.  $\text{H}_2$ -TPR profiles of the bulk  $\text{Co}_3\text{O}_4$  catalysts.
- 744 Figure 2. Relationship between the  $\text{Co}^{3+}/\text{Co}^{2+}$  and  $\text{O}_{\text{ads}}/\text{O}_{\text{latt}}$  molar ratios of the bulk
- 745  $\text{Co}_3\text{O}_4$  catalysts.
- 746 Figure 3. Light-off curves of the bulk  $\text{Co}_3\text{O}_4$  catalysts.
- 747 Figure 4. Relationship among the specific reaction rate and the  $\text{Co}^{3+}/\text{Co}^{2+}$  and
- 748  $\text{O}_{\text{ads}}/\text{O}_{\text{latt}}$  molar ratios of the bulk  $\text{Co}_3\text{O}_4$  catalysts.
- 749 Figure 5. XRD patterns of the  $x\text{Co}/\text{Al}_2\text{O}_3$  catalysts.
- 750 Figure 6. XPS profiles of the  $x\text{Co}/\text{Al}_2\text{O}_3$  catalysts.
- 751 Figure 7.  $\text{H}_2$ -TPR profiles of the  $x\text{Co}/\text{Al}_2\text{O}_3$  catalysts.
- 752 Figure 8. XRD patterns of the  $x\text{Ce}/\text{Co}_3\text{O}_4$  catalysts.
- 753 Figure 9. Raman spectra of the  $x\text{Ce}/\text{Co}_3\text{O}_4$  catalysts.
- 754 Figure 10. Relationship between  $\text{Co}^{3+}/\text{Co}^{2+}$  and  $\text{Ce}^{3+}/\text{Ce}^{4+}$  molar ratios of the
- 755  $x\text{Ce}/\text{Co}_3\text{O}_4$  catalysts.
- 756 Figure 11.  $\text{H}_2$ -TPR profiles of the  $x\text{Ce}/\text{Co}_3\text{O}_4$  catalysts.
- 757 Figure 12.  $\text{CH}_4$ -TPRe profiles of the  $x\text{Ce}/\text{Co}_3\text{O}_4$  catalysts.
- 758 Figure 13. Light-off curves of the  $x\text{Co}/\text{Al}_2\text{O}_3$  and  $x\text{Ce}/\text{Co}_3\text{O}_4$  catalysts.
- 759 Figure 14. Relationship between the  $\text{O}_2$  consumption at low temperatures ( $\text{CH}_4$ -
- 760 TPRE) and the specific reaction rate.

Catalyst	$S_{\text{BET}}$ , $\text{m}^2 \text{g}^{-1}$	$V_p$ , $\text{cm}^3 \text{g}^{-1}$	$D_p$ , $\text{\AA}$	$D_{\text{Co}_3\text{O}_4}$ , $\text{nm}$	Low-temperature $\text{H}_2$ uptake, $\text{mmol g}^{-1}$	High-temperature $\text{H}_2$ uptake, $\text{mmol g}^{-1}$	Relative $\text{H}_2$ uptake at low and high temperature	$\text{Co}^{3+}/\text{Co}^{2+}$ (XPS)	$\text{O}_{\text{ads}}/\text{O}_{\text{latt}}$ (XPS)
CC	14	0.09	257	63	4.3	12.4	0.35	1.96	0.40
HC	12	0.06	350	64	4.0	12.3	0.33	1.70	0.49
DC	5	0.02	353	84	3.9	12.8	0.30	1.50	0.57
COM	8	0.03	412	75	4.1	12.3	0.33	1.76	0.49

761

762

Table 1

Catalyst	T <sub>10</sub> , °C	T <sub>50</sub> , °C	T <sub>90</sub> , °C	Reaction rate, mmol CH <sub>4</sub> g <sub>Co</sub> <sup>-1</sup> h <sup>-1</sup>	E <sub>a</sub> , kJ mol <sup>-1</sup>
CC	335	430	505	1.85 <sup>a</sup>	74
HC	355	455	540	1.46 <sup>a</sup>	74
DC	365	480	575	1.07 <sup>a</sup>	74
COM	350	440	520	1.70 <sup>a</sup>	71
10Co/Al <sub>2</sub> O <sub>3</sub>	510	>600	>600	1.17 <sup>b</sup>	100
20Co/Al <sub>2</sub> O <sub>3</sub>	485	580	>600	1.17 <sup>b</sup>	92
30Co/Al <sub>2</sub> O <sub>3</sub>	440	550	>600	1.87 <sup>b</sup>	80
35Co/Al <sub>2</sub> O <sub>3</sub>	410	515	575	2.23 <sup>b</sup>	78
40Co/Al <sub>2</sub> O <sub>3</sub>	350	440	520	2.12 <sup>b</sup>	79
CeO <sub>2</sub>	>600	>600	>600	---	108
5Ce/Co <sub>3</sub> O <sub>4</sub>	340	435	515	1.81 <sup>a</sup>	78
10Ce/Co <sub>3</sub> O <sub>4</sub>	340	425	495	2.04 <sup>a</sup>	79
15Ce/Co <sub>3</sub> O <sub>4</sub>	340	435	500	1.97 <sup>a</sup>	79
20Ce/Co <sub>3</sub> O <sub>4</sub>	350	435	495	1.90 <sup>a</sup>	85

763 <sup>a</sup>Reaction rate calculated at 375 °C under differential conditions, methane conversion  
764 was below 20% over this set of Co<sub>3</sub>O<sub>4</sub>-based catalysts.

765 <sup>b</sup>Reaction rate calculated at 425 °C under differential conditions, methane conversion  
766 was below 20% over this set of Co<sub>3</sub>O<sub>4</sub>-based catalysts.

767

768

Table 2

Catalyst	% Co	$S_{\text{BET}}$ ,	$V_p$ ,	$D_p$ ,	$D_{\text{Co-phase}}$ ,	Low-temperature	High-temperature	% Co as	%Co as
		$\text{m}^2 \text{g}^{-1}$	$\text{cm}^3 \text{g}^{-1}$	$\text{\AA}$	nm	$\text{H}_2$ uptake, $\text{mmol g}^{-1}$	$\text{H}_2$ uptake, $\text{mmol g}^{-1}$	$\text{Co}_3\text{O}_4$	$\text{CoAl}_2\text{O}_4$
$\gamma\text{-Al}_2\text{O}_3$	-	136	0.55	123	-	-	-	-	-
10Co/ $\text{Al}_2\text{O}_3$	9.0	138	0.32	74	13	0.23	1.37	1.0	8.0
20Co/ $\text{Al}_2\text{O}_3$	21.7	120	0.34	94	16	1.75	2.35	7.7	14.0
30Co/ $\text{Al}_2\text{O}_3$	27.9	108	0.29	89	29	3.11	2.40	13.7	14.2
35Co/ $\text{Al}_2\text{O}_3$	33.1	95	0.23	82	35	4.62	2.28	20.0	13.1
40Co/ $\text{Al}_2\text{O}_3$	40.5	84	0.23	90	34	6.36	2.37	27.0	13.5

769

770

Table 3

Catalyst	$S_{\text{BET}}$ , $\text{m}^2 \text{g}^{-1}$	$V_p$ , $\text{cm}^3 \text{g}^{-1}$	$D_p$ , $\text{\AA}$	$D_{\text{Co}_3\text{O}_4}$ , $\text{nm}$	Ce/Co molar ratio	$\text{Co}_3\text{O}_4$ cell size, $\text{\AA}$
CC	14	0.09	257	63	0	8.0958
5Ce/ $\text{Co}_3\text{O}_4$	33	0.14	155	32	0.033 (0.030)	8.0980
10Ce/ $\text{Co}_3\text{O}_4$	35	0.14	143	29	0.063 (0.064)	8.0982
15Ce/ $\text{Co}_3\text{O}_4$	30	0.11	176	38	0.100 (0.101)	8.0948
20Ce/ $\text{Co}_3\text{O}_4$	34	0.11	153	35	0.142 (0.143)	8.0940
$\text{CeO}_2$	12	0.05	235	-	-	-

Values in brackets correspond to the nominal Ce/Co molar ratios

771

772

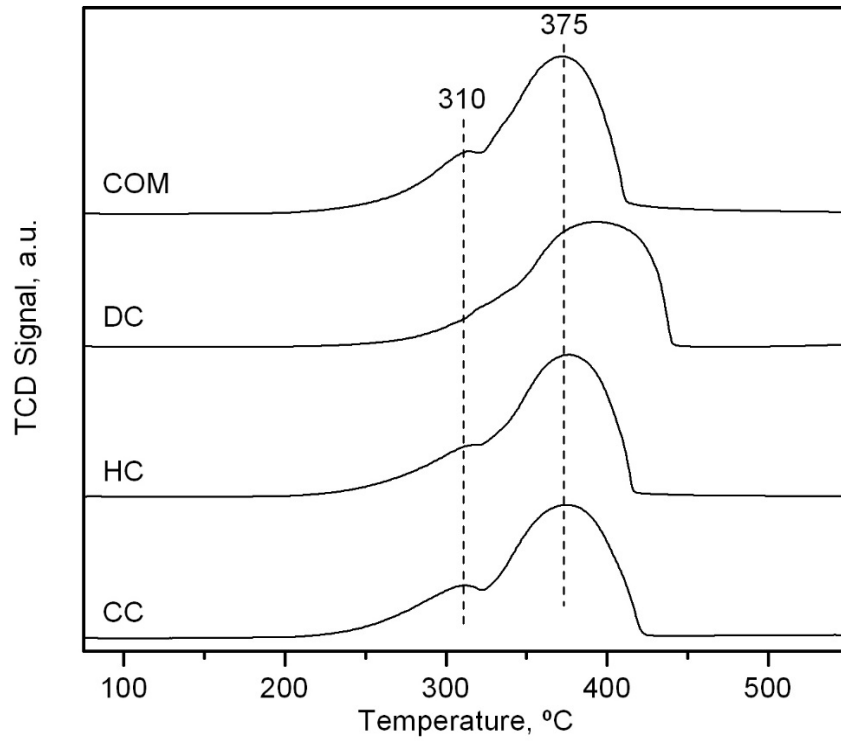
Table 4

Catalyst	H <sub>2</sub> -TPR			CH <sub>4</sub> -TPRe		
	Low-temperature peak, mmol g <sup>-1</sup>	High-temperature peak, mmol g <sup>-1</sup>	Relative H <sub>2</sub> uptake at low and high temperature	Low-temperature peak, °C	High-temperature peak, °C	Relative CO <sub>2</sub> production at low and high temperature
CC	4.29	12.41	0.35	485	620	0.56
5Ce/Co <sub>3</sub> O <sub>4</sub>	3.80	11.38	0.33	480	680	0.54
10Ce/Co <sub>3</sub> O <sub>4</sub>	3.76	10.36	0.36	460	605	0.66
15Ce/Co <sub>3</sub> O <sub>4</sub>	3.42	9.68	0.35	500	675	0.61
20Ce/Co <sub>3</sub> O <sub>4</sub>	3.15	9.20	0.34	510	695	0.63

773

774

Table 5

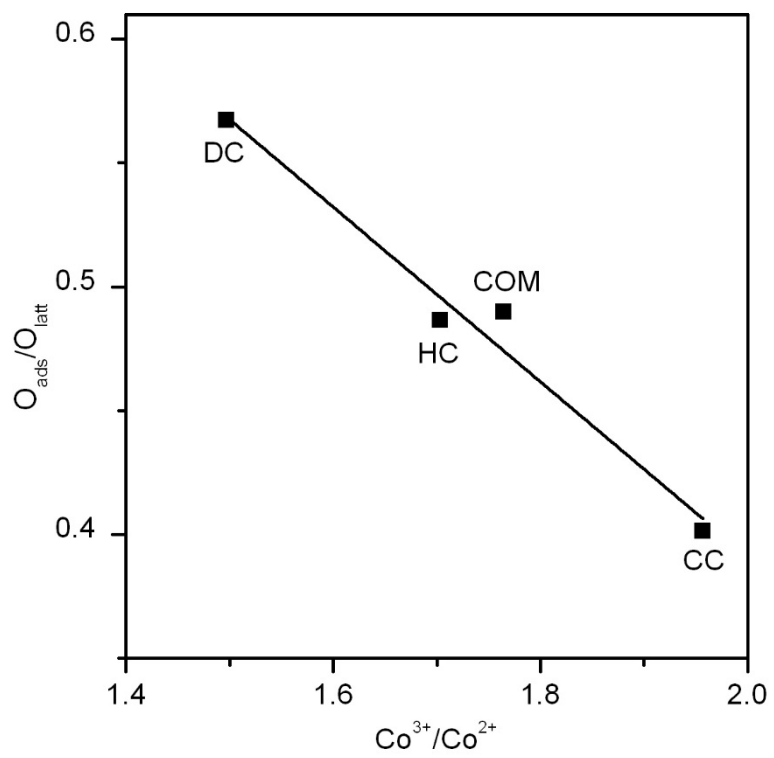


775

776

777

Figure 1

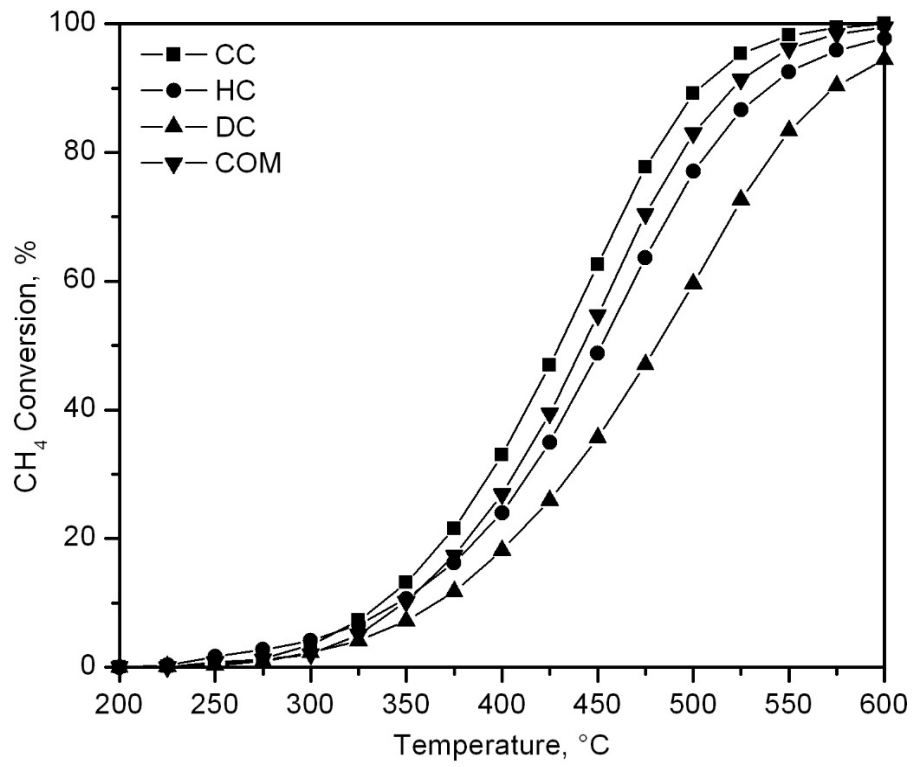


778

779

780

Figure 2

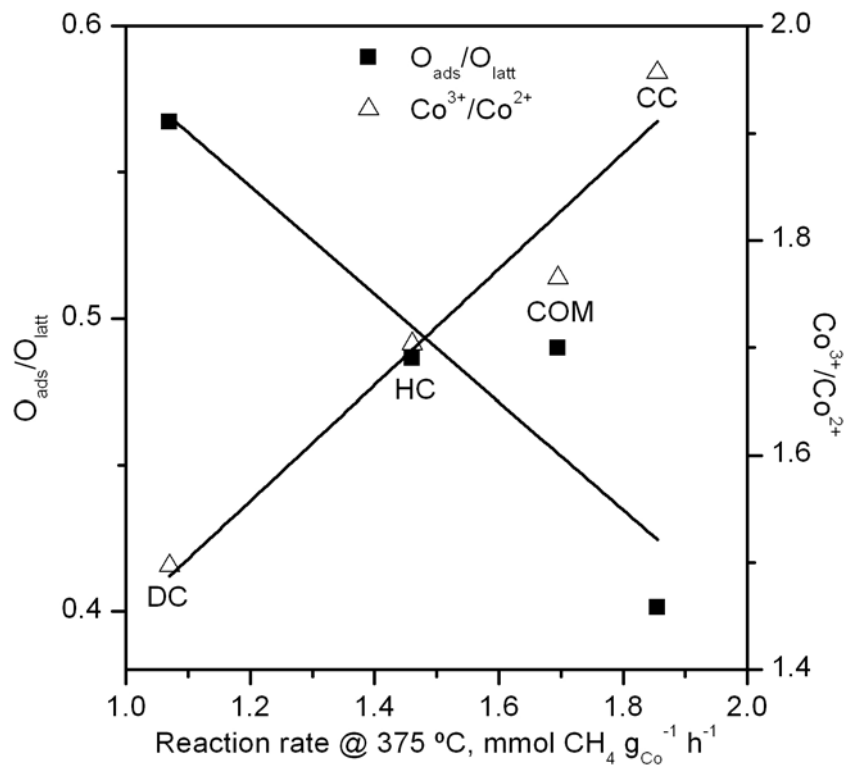


781

782

783

Figure 3

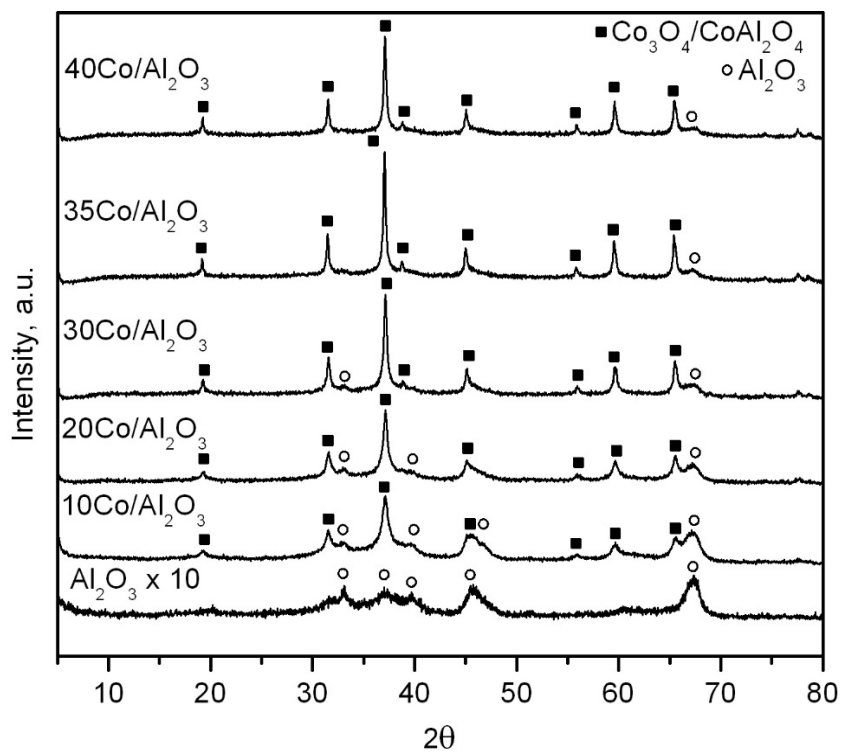


784

785

786

Figure 4

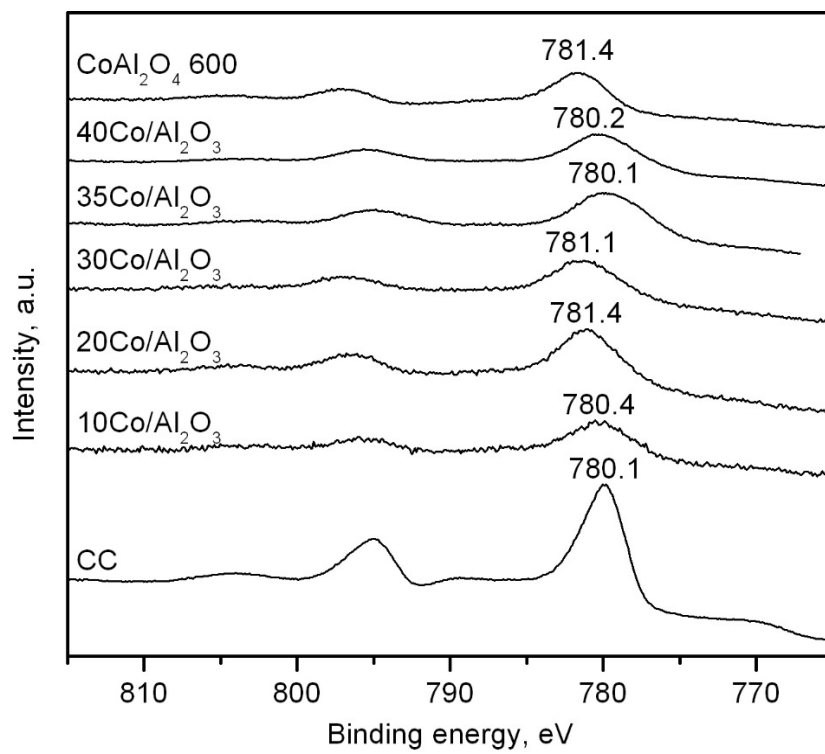


787

788

789

Figure 5

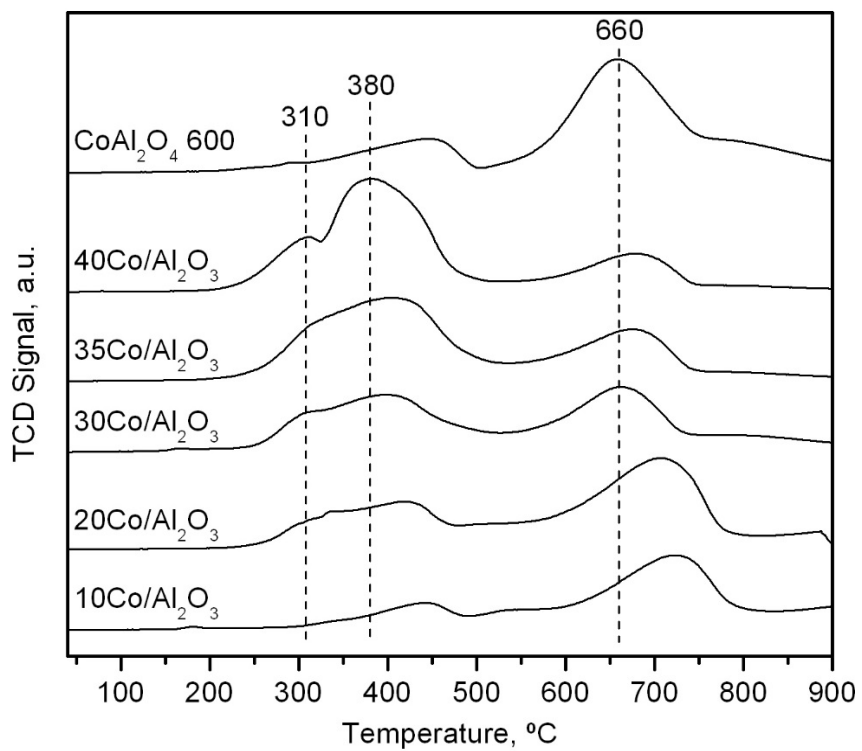


790

791

792

Figure 6

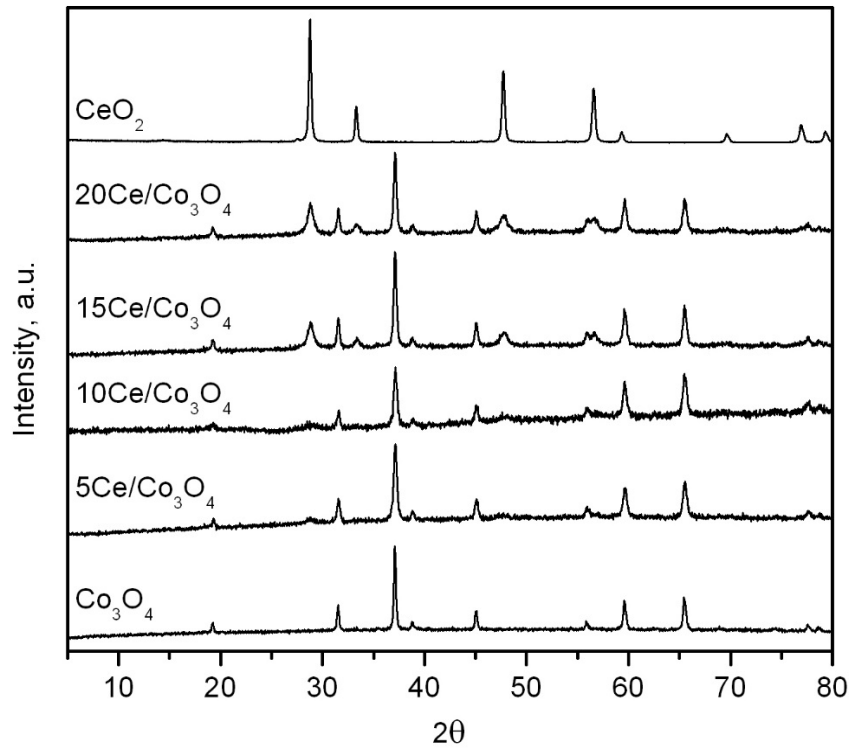


793

794

795

Figure 7

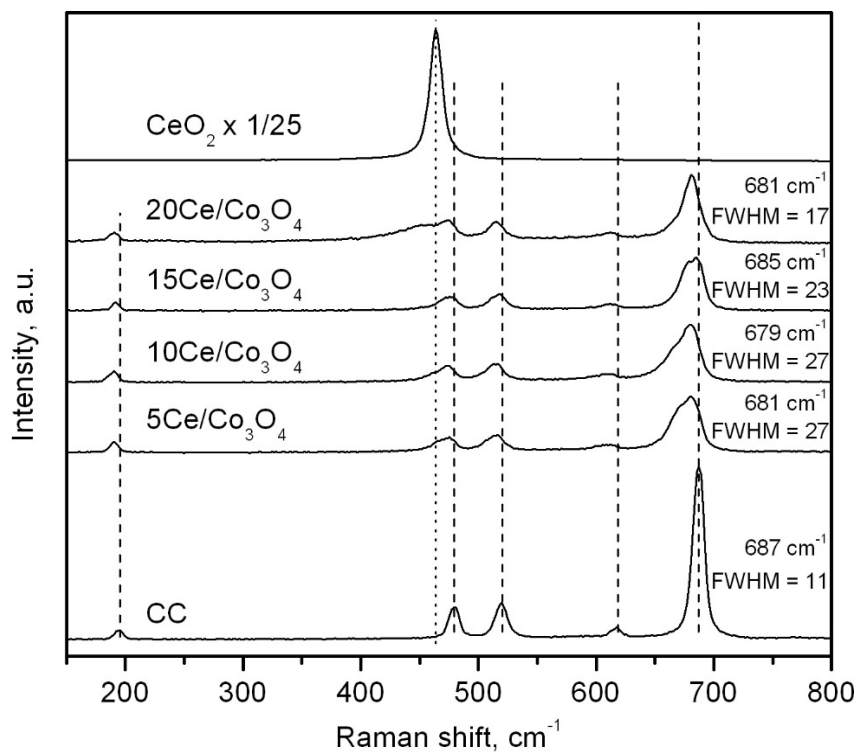


796

797

798

Figure 8

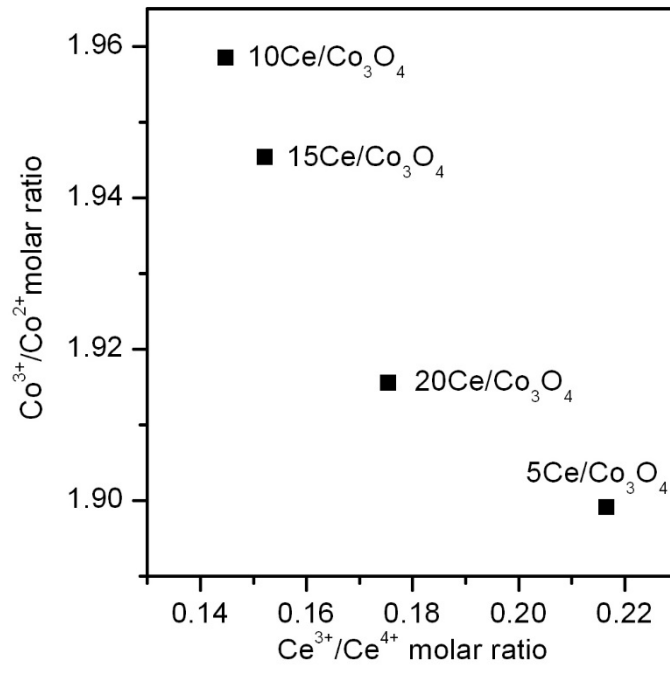


799

800

801

Figure 9

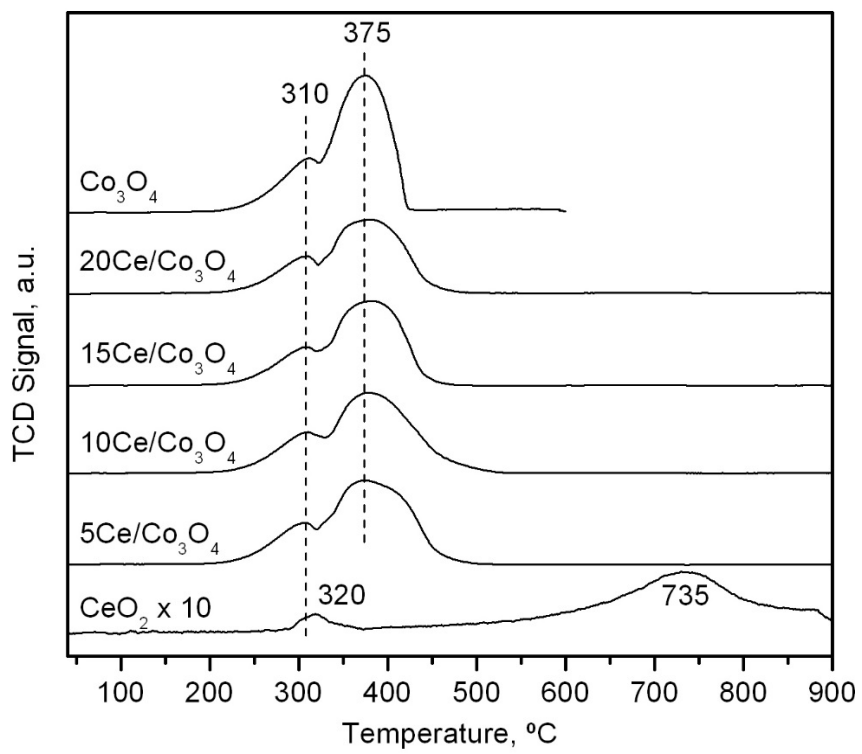


802

803

804

Figure 10

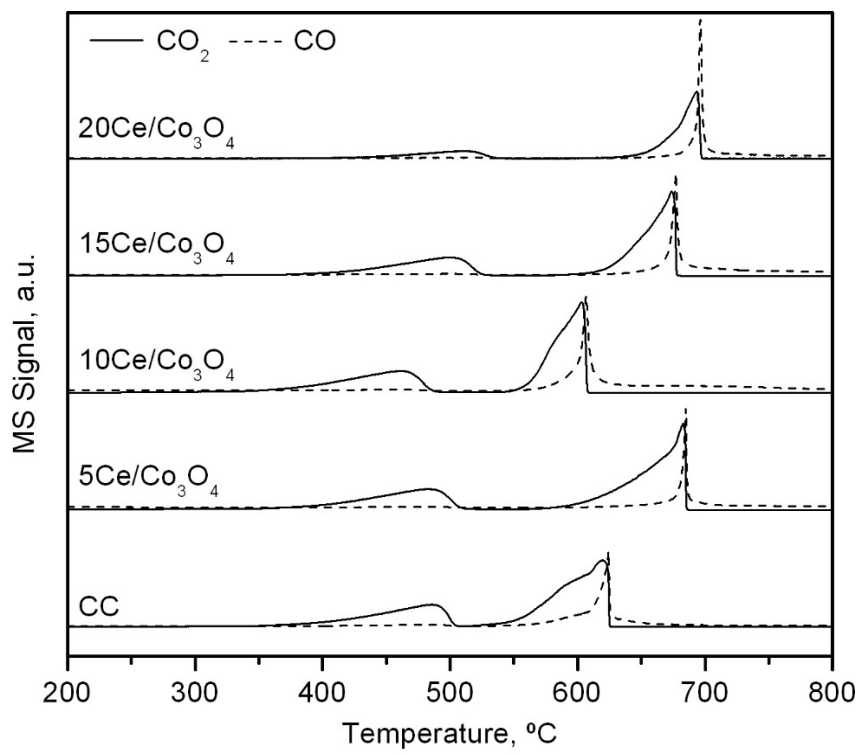


805

806

807

Figure 11

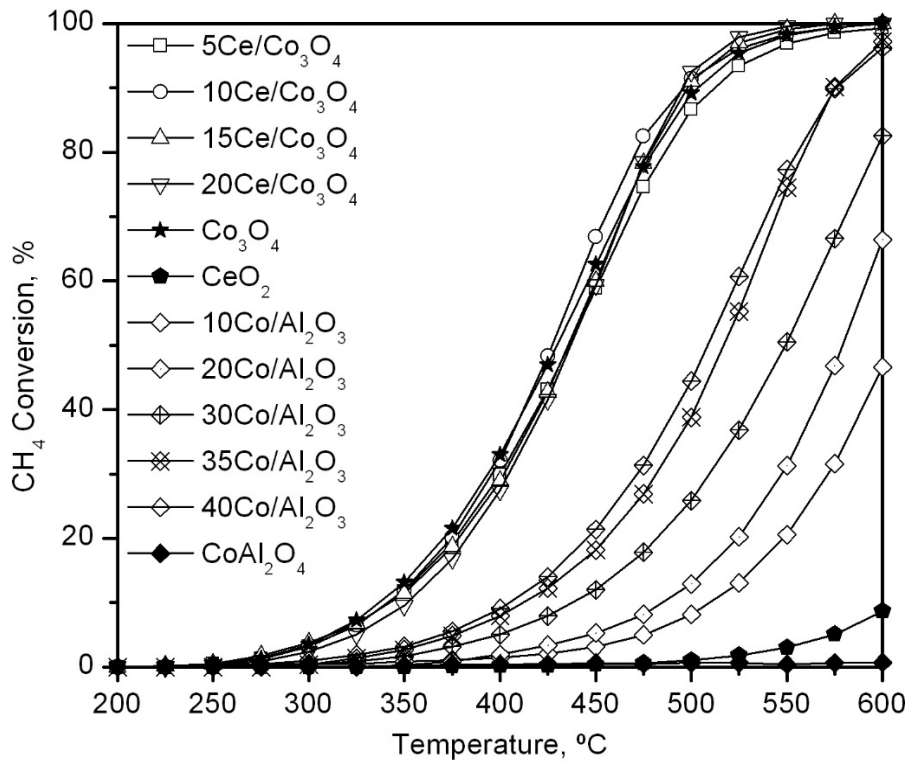


808

809

810

Figure 12

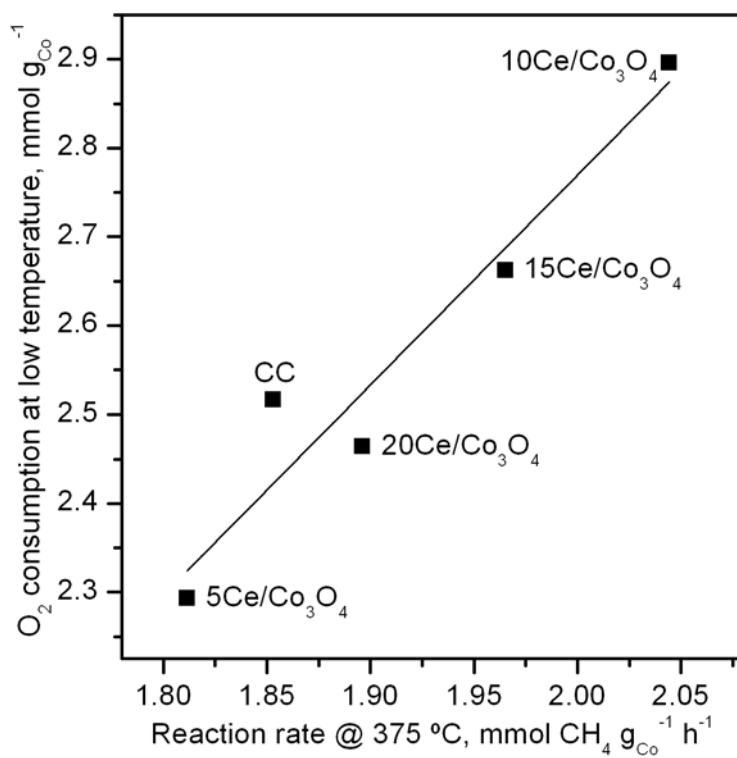


811

812

813

Figure 13



814

815

Figure 14